Research Square

Preprints are preliminary reports that have not undergone peer review.
They should not be considered conclusive, used to inform clinical practice,
or referenced by the media as validated information.

Entanglement Redistribution in anAtom–Plasmon–Mechanical System with ModulatedCoupling

Syed Jamal Anwar

sjamalanwar@gmail.com

Quaid-i-Azam University

S. Abdul Khalek S. Abdul Khalek

Taif University

Research Article

Keywords: quantum plasmonics; effective bosonic mode; optomechanics; negativity; prescribed atomic motion; transition detuning

Posted Date: November 16th, 2026

DOI: https://doi.org/10.21203/rs.3.rs-11567776/v1

License: This work is licensed under a Creative Commons Attribution 4.0 International License.
Read Full License

Additional Declarations: No competing interests reported.

Entanglement Redistribution in an Atom–Plasmon–Mechanical System with Modulated Coupling

S. Jamal Anwar[1,*] and S. Abdul Khalek[2]

[1]Department of Physics, Quaid-i-Azam University, Islamabad 45320, Pakistan

[2]Department of Mathematics and Statistics, College of Science,

Taif University, P.O. Box 11099, Taif 21944, Saudi Arabia

[*]Corresponding author: sjamalanwar@gmail.com

S. Abdul Khalek: sabotalb@tu.edu.sa

Abstract

We investigate how a mechanical degree of freedom modifies entanglement generated by coherent atom–mode exchange. The model contains a two-level atom, one effective plasmonic bosonic mode, and a mechanical oscillator. Atom–mode exchange follows a prescribed standing-wave modulation, while the mechanical oscillator experiences an occupation-dependent force. Starting from a separable atomic superposition and two coherent states, we propagate the full state and evaluate the negativity of each reduced pair. In the reference calculation ($0 \leq \omega_m t \leq 30$), the sampled atom–mode, atom–mechanics, and mode–mechanics maxima are 0.466, 0.0920, and 0.263, attained at different times. Parameter sweeps show that a change which raises a short-lived maximum may lower the time-window average; stronger mechanical coupling, in particular, has a much clearer effect on the pairs involving the oscillator than on the mean atom–mode negativity. The atomic inversion, purity, and von Neumann entropy supply complementary information about the atom versus the remaining two subsystems. A 17-point initial-phase scan gives mean atomic entropies between 0.4456 and 0.7017 bits with unchanged Hamiltonian parameters. Basis-size and integration-step comparisons test numerical consistency. Because atomic detuning and a Zeeman-type shift appear through one effective offset, they are not independent controls in this model. These results characterize finite-time, unitary dynamics of a single effective mode, not microscopic plasma response or entanglement robustness in a dissipative device.

Keywords: quantum plasmonics; effective bosonic mode; optomechanics; negativity; prescribed atomic motion; transition detuning

1 Introduction

The question of which correlations survive when part of a quantum system is ignored has been central to entanglement theory since Einstein, Podolsky and Rosen, Schrödinger, and Bell [1–3]. It is particularly delicate in a three-component system. An entropy calculated for the atom describes its relationship with everything else, whereas the atom and just one of the other components

generally form a mixed state. We therefore need a mixed-state test for each reduced pair [4–12]. Our choice is negativity. We analyze it pair by pair, without importing three-qubit monogamy identities into systems that contain bosonic modes.

Coherent exchange between a two-level atom and a quantized mode is described by the Jaynes–Cummings Hamiltonian in the rotating-wave regime [13]. Its occupation-dependent oscillation frequencies explain collapse and revival and contribute to the generation of nonclassical fields and atom–field correlations [14–17, 21]. Related two-photon and mixed-state settings show why one must distinguish atomic entropy from the entanglement retained by a particular pair [18–20]. Here that distinction matters because the atom exchanges excitations with one bosonic mode, while a second bosonic subsystem is coupled indirectly.

Experiments in quantum plasmonics have shown that converting photonic excitations into confined surface modes need not erase quantum interference or single-quantum signatures [22–25, 29–31, 33]. The theoretical literature addresses emitter–plasmon coupling, mediated qubit entanglement, and nonlinear plasmonic processes [26–28, 34–36]. Distillation and teleportation proposals highlight possible information-processing uses [32, 38]. Entangled photons generated through plasma four-wave mixing belong to a different microscopic setting [37]; they should not be confused with the effective single-mode interaction studied below.

The label "quantum plasma" needs some care. In a microscopic plasma calculation, degeneracy, quantum diffraction, spin, screening, and the electronic distribution can enter the collective response [39–43]. None of these quantities is evolved here. We retain a single quantized collective resonance and treat its frequency and couplings as effective parameters. This reduction makes a tractable three-subsystem calculation possible, but it also means that density-dependent or material-specific predictions cannot be extracted from the present plots.

Radiation pressure provides a well-established route from bosonic occupation to mechanical displacement. It underlies optomechanical bistability, cooling, strong coupling, and quantum-state manipulation [44–52]. Atom–light–mechanical correlations have also been investigated in hybrid systems [53–60]. These precedents help place the present model in context. The driven, dissipative atom–light–mirror description of Ref. [56], for example, is different from the closed, single-atom evolution used here; Ref. [55] likewise addresses an atom–oscillator interface rather than the three-pair negativity scan considered here.

Two recent studies help define what this calculation can and cannot show. Multimode effects in plasmonic nanocavities were examined by Crookes, Yuen, and Demetriadou [61, 62], while Medina-Armendariz and colleagues treated a three-level atom–optomechanical model with a master equation and squeezed reservoir [63]. Neither study supplies the dynamics of the Hamiltonian used here. They do, however, make the missing ingredients conspicuous: our model has neither a multimode plasmonic response nor reservoir-induced loss. The narrower question pursued in this paper is how a single effective bosonic mediator distributes NPT entanglement among its three possible pairs when exchange, conditional displacement, initial phase, and prescribed motion are changed.

The structure of the Hamiltonian suggests an asymmetry worth testing. The atom can exchange excitations with the effective plasmon mode, but it has no direct interaction with the mechanical oscillator. Mechanical motion instead depends on mode occupation. Thus a nonzero atom–mechanics negativity, if it develops, is mediated by the mode; the mode–mechanics pair follows a different interaction pathway. We calculate all three reductions rather than using the

atom–mode pair as a proxy for the others.

There is also no unique way to rank a time-dependent entanglement trace. Its maximum identifies an exceptional instant; its mean over a fixed interval describes a sustained response; its peak time indicates when the strongest sampled transient occurs. We report all three, together with running means, because the rankings can disagree. Comparisons are made within each pair: a boson–boson negativity and a qubit–boson negativity do not share the same upper bound. Zero negativity is interpreted cautiously in the truncated mixed-state dimensions considered here.

We use a single initial product state as a reference and vary one parameter at a time: atom–mode exchange, occupation–displacement coupling, effective transition offset, or the frequency of a prescribed spatial modulation. A separate phase scan changes the preparation rather than the Hamiltonian. Atomic population, purity, and entropy are calculated to examine the distinct bipartition $A : (PM)$. We retain only physically distinct parameter settings in the summary plots and test the reported curves against larger basis sizes and smaller integration steps. No material-specific plasma dispersion or device efficiency is inferred.

2 Effective Model

2.1 Collective mode and mechanical coupling

The degrees of freedom used in the calculation are shown in Figure 1. We describe the central oscillator as a "plasma" or "plasmon" mode to indicate a quantized collective excitation, but represent it by a single bosonic operator. The calculation is therefore an effective resonance model; it does not solve a quantum-hydrodynamic or kinetic plasma equation. In particular, the frequency and coupling coefficients below cannot be identified with material-dependent plasma quantities until a specific mode profile and medium response have been supplied.

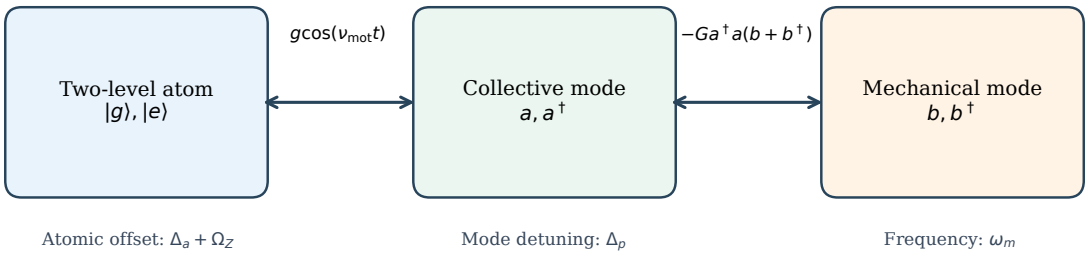


Figure 1: Schematic of the effective three-part model. The atom exchanges excitations with one quantized collective mode through the modulated coupling $gf(t)$; the mode occupation couples to mechanical position. The atomic controls modify one transition offset. Boxes denote mathematical degrees of freedom, not an experimentally specified device layout.

The atom has states $|e\rangle$ and $|g\rangle$, with $\sigma_+ = |e\rangle\langle g|$, $\sigma_- = \sigma_+^\dagger$, and $\sigma_z = |e\rangle\langle e| - |g\rangle\langle g|$. The collective mode has frequency ω_a and annihilation operator a; the mechanics has frequency ω_m and operator b. The infinite-dimensional operators satisfy $[a, a^\dagger] = [b, b^\dagger] = 1$. Their finite numerical representations approximate these relations away from the highest retained Fock state.

For a homogeneous medium with an effective background dielectric constant, the bulk plasma-frequency scale is

$$\omega_{\mathrm{p}} = \sqrt{\frac{n_e e^2}{m_e \epsilon_0 \epsilon_{\mathrm{eff}}}}. \tag{1}$$

Boundary conditions, geometry, and dispersion determine the actual confined-mode frequency. Equation 1 supplies context for ω_a; it is not a mode derivation and is not used to introduce an electron-density dependence into the plotted curves.

An occupation–displacement coupling arises phenomenologically by expanding a mode frequency with displacement. With $x = x_{\mathrm{zpf}}(b + b^\dagger)$ and $x_{\mathrm{zpf}} = \sqrt{\hbar/(2m_{\mathrm{eff}}\omega_m)}$, the convention $\omega_a(x) = \omega_a(0) - Gx/x_{\mathrm{zpf}}$ gives

$$G = -x_{\mathrm{zpf}} \left.\frac{\partial \omega_a}{\partial x}\right|_{x=0}. \tag{2}$$

The sign depends on the displacement convention. Likewise, the magnitude of a dipole exchange would follow $g = |\boldsymbol{d}_{eg} \cdot \boldsymbol{E}_{\mathrm{zpf}}|/\hbar$ for an appropriately normalized mode field. Neither this field nor a mechanical geometry is specified here; g and G are effective theoretical parameters. The single-mode approximation is best viewed as a controlled effective description only if the selected resonance is sufficiently isolated from neighboring modes and relevant loss rates. In a specified system, one would need the electromagnetic mode normalization and dipole overlap to infer g, the optomechanical frequency gradient to infer G, and a linewidth and bath temperature to assess whether the plotted interval is accessible. In particular, the optomechanical term does not itself constitute a direct atom–mechanics interaction. If $g = 0$, the atomic state evolves locally and remains unentangled with the joint mode–mechanics system for the chosen product input. If $G = 0$, the mechanics evolves independently, so both entanglement measures containing the mechanical oscillator remain zero in the exact model. These limiting cases are useful physical and numerical controls.

2.2 Hamiltonian and prescribed trajectory

With $\hbar = 1$, after the rotating-wave approximation on the atomic exchange, the laboratory-frame model is

$$\begin{aligned} H_{\mathrm{lab}}(t) = {} & \omega_a a^\dagger a + \omega_m b^\dagger b + \frac{\omega_0 + \Omega_Z}{2}\sigma_z - G a^\dagger a (b + b^\dagger) \\ & + g f(t)(a\sigma_+ + a^\dagger \sigma_-). \end{aligned} \tag{3}$$

The exchange approximation requires its populated-sector coupling scales and modulation frequency to be small compared with the optical or other carrier frequencies. A single-mode description also requires suitable separation from other resonances. The chosen dimensionless parameters do not independently demonstrate these inequalities for a device.

Transforming with a common reference frequency ω_L gives

$$\begin{aligned} H(t) = {} & \Delta_p a^\dagger a + \frac{\Delta_a + \Omega_Z}{2}\sigma_z + \omega_m b^\dagger b - G a^\dagger a (b + b^\dagger) \\ & + g f(t)(a\sigma_+ + a^\dagger \sigma_-), \end{aligned} \tag{4}$$

where $\Delta_p = \omega_a - \omega_L$ and $\Delta_a = \omega_0 - \omega_L$. The reference frequency is a change of frame, not a

classical laser drive. Inspection of Eq. 4 shows that the atomic shift and bare atomic detuning appear only through their sum. The atom–mode offset can therefore be written as

$$\delta = \Delta_a + \Omega_Z - \Delta_p. \tag{5}$$

Thus Ω_Z and Δ_a are exactly interchangeable in this Hamiltonian when their sum is fixed. Here Ω_Z is an abstract Zeeman-type transition offset. For a specified transition in a weak-field linear regime, it could be related to field by $\Omega_Z = \mu_B B(\mathfrak{g}_e m_e - \mathfrak{g}_g m_g)/\hbar$, with state-dependent Landé factors $\mathfrak{g}_{e,g}$. Changes of the collective mode with magnetic field are neglected.

We prescribe the classical trajectory $z(t) = vt$ across an ideal standing-wave profile,

$$f(t) = \cos(\nu_{\mathrm{mot}} t), \qquad \nu_{\mathrm{mot}} = kv. \tag{6}$$

At zero motion frequency, $f = 1$. Its sign reversals represent local exchange phases. Figure 2 illustrates the three profiles used in the motion scan; for the stationary setting the coupling never passes through zero, whereas for moving settings the exchange is periodically switched off and its sign is reversed. Since a full evolution involves time ordering together with the free and dispersive dynamics, a cosine profile cannot generally be replaced by its simple time average. The atom's

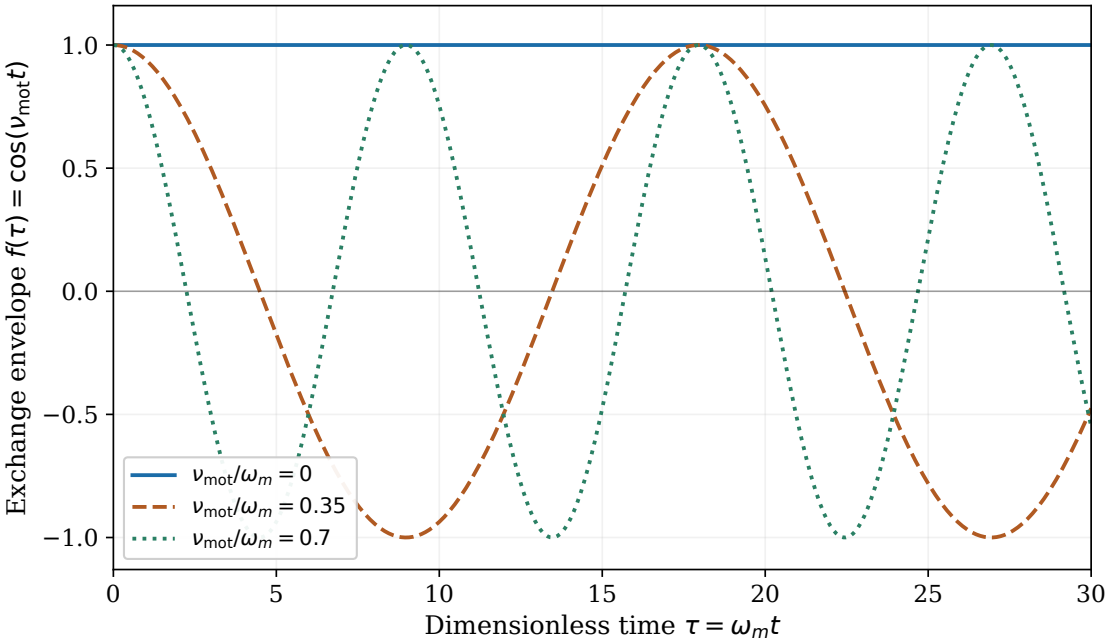


Figure 2: Prescribed dimensionless coupling envelopes $f(\tau) = \cos[(\nu_{\mathrm{mot}}/\omega_m)\tau]$ for the three motion-scan settings. The profiles are specified inputs to the Schrödinger equation, not simulated atomic trajectories.

translational state is not quantized: recoil, acceleration, wavepacket spreading, and back-action on v are neglected. A localized mode would generally require an additional spatial envelope; the constant-amplitude cosine assumes an interaction region supporting the prescribed profile over the full plotted interval.

2.3 Initial state and exact constraints

The separable initial state is

$$|\Psi(0)\rangle = \left[\cos\left(\frac{\theta}{2}\right)|g\rangle + e^{i\phi}\sin\left(\frac{\theta}{2}\right)|e\rangle\right] \otimes |\alpha\rangle_P \otimes |\beta\rangle_M. \tag{7}$$

The coherent-state expansion is $|\gamma\rangle = e^{-|\gamma|^2/2}\sum_{n=0}^{\infty}\gamma^n|n\rangle/\sqrt{n!}$. Each finite-basis coherent state is renormalized. We choose the reference coherent amplitude $\alpha = 1.30$ to be real and positive. Relative to that convention, the phase ϕ sets the atomic coherence with respect to the collective-mode phase. Changing ϕ while holding α fixed is an independent initial-state control; a simultaneous local rephasing of the atomic and collective-mode bases is only a convention change and leaves entanglement invariant. The evolution obeys

$$i\partial_t|\Psi(t)\rangle = H(t)|\Psi(t)\rangle, \qquad \rho(t) = |\Psi(t)\rangle\langle\Psi(t)|. \tag{8}$$

Loss, mechanical damping, thermal reservoirs, and collision-induced dephasing are absent. This is a pure-state, time-dependent unitary model. It conserves excitation,

$$Q = a^\dagger a + |e\rangle\langle e|, \qquad [Q, H(t)] = 0. \tag{9}$$

A common shift of both detunings adds a multiple of Q plus a scalar. Since the associated phase rotation is local with respect to the three subsystems, it leaves their negativities invariant. Energy, however, need not be conserved:

$$\frac{d}{dt}\langle H\rangle = \left\langle\frac{\partial H}{\partial t}\right\rangle = -g\nu_{\rm mot}\sin(\nu_{\rm mot}t)\langle a\sigma_+ + a^\dagger\sigma_-\rangle. \tag{10}$$

The prescribed modulation can perform work; unitary evolution does not imply an autonomous model of atomic translation.

2.4 Conditional displacement

Completing the square in the mechanical terms yields

$$\omega_m b^\dagger b - Gn_P(b + b^\dagger) = \omega_m\left(b^\dagger - \frac{G}{\omega_m}n_P\right)\left(b - \frac{G}{\omega_m}n_P\right) - \frac{G^2}{\omega_m}n_P^2, \tag{11}$$

where $n_P = a^\dagger a$. With the exchange switched off, the mechanical amplitude in a plasma-number sector is

$$\beta_n(t) = \beta e^{-i\omega_m t} + \frac{Gn}{\omega_m}(1 - e^{-i\omega_m t}). \tag{12}$$

Even when the mechanical coherent state is weakly occupied initially, a larger G can drive its conditional states farther from the origin. The numerical mechanical cutoff must therefore be reassessed at each coupling. The $n = 0$ component undergoes free oscillation; components with $n > 0$ acquire occupation-dependent displacements. A superposition of mode-number sectors can thus develop correlations between the mode and the mechanical oscillator. For two such sectors,

the amplitude separation is

$$\beta_n(t) - \beta_{n'}(t) = \frac{G(n-n')}{\omega_m}(1 - e^{-i\omega_m t}), \tag{13}$$

whose magnitude oscillates with the mechanical period. This conditional separation provides a useful physical picture of the P:M correlation, but its magnitude alone is not an entanglement measure. The joint mode–mechanics state also acquires phase information, and the simultaneous exchange with the atom makes the reduced pair mixed. The uncoupled displaced-sector energy difference between $|e, n, q\rangle$ and $|g, n+1, q'\rangle$ includes

$$\delta + \frac{G^2}{\omega_m}(2n+1) + \omega_m(q - q'). \tag{14}$$

Exchange connects differently displaced mechanical states, and $\cos(\nu t)$ adds modulation frequencies $\pm\nu$. These ingredients provide a possible explanation of the nonmonotonic response. A dressed-state or Floquet-spectrum identification of the particular interference pathways is not established by the curves alone. The effective nonlinear Hamiltonian is used at low occupation and finite time; its negative n_P^2 shift is not a globally stable material model at arbitrarily large occupation.

3 Pairwise Negativity and Numerical Method

To make the entanglement calculation explicit, write the pure state in the truncated product basis as

$$|\Psi(t)\rangle = \sum_{s\in\{g,e\}} \sum_{n=0}^{N_p-1} \sum_{q=0}^{N_m-1} C_{snq}(t)|s, n, q\rangle, \qquad \sum_{snq} |C_{snq}|^2 = 1. \tag{15}$$

The probability amplitudes are propagated according to Eq. 8; thus no Born–Markov or Lindblad approximation is applied. The three pair reductions are formed by summing over the omitted index rather than constructing a very large full density matrix. For example,

$$(\rho_{AP})_{sn,s'n'} = \sum_q C_{snq} C^*_{s'n'q}, \tag{16}$$

$$(\rho_{AM})_{sq,s'q'} = \sum_n C_{snq} C^*_{s'nq'}, \tag{17}$$

$$(\rho_{PM})_{nq,n'q'} = \sum_s C_{snq} C^*_{sn'q'}. \tag{18}$$

These equations show why a pure total state need not yield pure states for the three pairs. Only for special factorized states would tracing over the third subsystem leave a pure pair.

The reduced pair states are

$$\rho_{AP} = \mathrm{Tr}_M\, \rho, \qquad \rho_{AM} = \mathrm{Tr}_P\, \rho, \qquad \rho_{PM} = \mathrm{Tr}_A\, \rho. \tag{19}$$

Although the total state is pure, each pair is generally mixed. Atomic entropy concerns the bipartition $A : (PM)$ and cannot be assigned to $A : P$ alone. Partial transpose is defined by

$$\langle i\mu|\rho_{XY}^{T_X}|j\nu\rangle = \langle j\mu|\rho_{XY}|i\nu\rangle. \tag{20}$$

The negativity is [9]

$$\mathcal{N}_{X:Y} = \frac{\|\rho_{XY}^{T_X}\|_1 - 1}{2} = \sum_{\lambda_r<0} |\lambda_r|. \tag{21}$$

Positive negativity establishes NPT entanglement. Zero negativity does not generally imply separability in the dimensions used here [5,6]. For a $d_X \times d_Y$ state, the maximum is $(\min(d_X, d_Y) - 1)/2$, giving 1/2 for AP and AM. The PM pair has a different dimensional scale; its negativity can exceed 1/2. Pairwise negativities are not additive or conserved, so their sum is not an entanglement budget or a tripartite entanglement measure. A positive $\mathcal{N}_{AP}$, for example, detects a negative eigenvalue of $\rho_{AP}^{T_A}$ even though ρ_{AP} may have nonzero entropy. Conversely, the atom can have nonzero reduced-state entropy because it is entangled across $A{:}(PM)$ without specifying how much of that correlation belongs to $A{:}P$ or $A{:}M$. No atomic entropy, quantum Fisher information, or genuine-tripartite entanglement witness is inferred from the three negativity curves.

A practical finite-basis calculation obtains the eigenvalues of each Hermitian partially transposed reduced matrix, sums only the magnitudes of its negative eigenvalues, and checks that small negative numerical noise is below the declared tolerance. The maximum possible atomic-pair negativity is 1/2, but the $P{:}M$ maximum depends on the smaller bosonic Hilbert-space dimension and can be much larger. Therefore the values in Figures 3–13 are compared within the same pair when assessing a parameter response.

3.1 Atomic information diagnostics

In addition to the three two-body reductions, we form the atomic marginal $\rho_A = \mathrm{Tr}_{PM} |\Psi\rangle\langle\Psi|$, a 2×2 state obtained without further approximations. Its excited-state population, inversion, purity and von Neumann entropy are

$$P_e(\tau) = \langle e|\rho_A(\tau)|e\rangle, \qquad W(\tau) = \mathrm{Tr}[\rho_A(\tau)\sigma_z] = 2P_e(\tau) - 1, \tag{22}$$

$$\mathcal{P}_A(\tau) = \mathrm{Tr}\,\rho_A^2(\tau), \qquad S_A(\tau) = -\,\mathrm{Tr}[\rho_A(\tau)\log_2\rho_A(\tau)]. \tag{23}$$

We also record the linear entropy $L_A = 1 - \mathcal{P}_A$. For an atomic qubit, $0 \le S_A \le 1$ bit and $1/2 \le \mathcal{P}_A \le 1$; $\rho_A(0)$ is pure so $S_A(0) = L_A(0) = 0$. Since the full three-body state remains pure, S_A measures bipartite entanglement across $A : (PM)$, *not* pair entanglement of $A : P$ or $A : M$. This distinction is particularly sharp when $G = 0$: $A : M$ is exactly separable despite possible atomic entropy generated by the $A : P$ interaction. Inversion and occupation also provide a direct check of $\langle Q\rangle = \langle a^\dagger a\rangle + P_e$.

We integrate the product-basis amplitude tensor C_{snq} with a fourth-order Runge–Kutta scheme. The omitted subsystem is traced out by forming a Gram matrix of the remaining amplitudes, avoiding construction of the full density matrix. For the $P{:}M$ negativity, a local singular-vector rotation can reduce the mechanical matrix dimension; squared amplitudes below 10^{-10} are omitted in that compression. If their total discarded weight is ϵ, the saved estimate $N_p\sqrt{\epsilon} + \epsilon/2$ bounds the associated change in negativity. The propagation itself still uses the full chosen basis. We compare compressed and uncompressed partial transposes in the validation tests, sum eigenvalues only below -10^{-11}, and monitor the norm before renormalization. These numerical cutoffs are implementation checks, not physical thresholds.

The reference basis contains $N_p = 19$ plasmon and $N_m = 28$ mechanical states, and the principal RK4 step is 0.0125. Every negativity trajectory is compared at identical output times with a

Table 1: Reference parameters. Frequencies are in units of ω_m.

Quantity	Value	Meaning
N_p, N_m	$19, 28$	Retained bosonic states
α, β	$1.30, 0.35$	Coherent amplitudes
θ, ϕ	$\pi/2, \pi/4$	Atomic angles
g/ω_m	0.25	Exchange strength
G/ω_m	0.08	Displacement coupling
Ω_Z/ω_m	0.30	Transition offset
$\nu_{\mathrm{mot}}/\omega_m$	0.35	Prescribed modulation
$\Delta_p/\omega_m, \Delta_a/\omega_m$	$0, 0$	Bare detunings
Time window	$0 \le \tau \le 30$	$\tau = \omega_m t$
Integration/output steps	0.0125/0.025	1201 recorded times

$(21, 32)$ basis and, separately, with a step of 0.025. Table 2 reports the largest absolute pointwise differences across the scans. The practical target is 10^{-4}, which all listed comparisons satisfy. This establishes stability against the tested changes, not a mathematically certified error bound for an infinite-dimensional problem. Norm preservation is necessary but insufficient: truncation and partial-transpose errors must be checked separately.

Table 2: Largest absolute negativity differences across all tested parameter settings and recorded times.

Comparison	AP	AM	PM
Larger basis	1.95×10^{-8}	9.89×10^{-9}	4.36×10^{-5}
Integration step	1.86×10^{-8}	3.89×10^{-8}	2.51×10^{-7}

Across the final runs, the largest plasma and mechanical boundary populations are 2.30×10^{-12} and 1.03×10^{-10}. The maximum norm defect before a normalization step is 1.22×10^{-13} and the maximum deviation in $\langle Q \rangle$ is 2.11×10^{-10}. Reduced-state trace and Hermiticity defects are also saved. Bell and product-state tests give negativities 0.5 and zero. Stationary-atom evolution is compared with exact matrix-exponential propagation at the same finite basis in the reproducibility checks. At $G = 0$, the mechanical subsystem must factorize and its pair negativities vanish; residual numerical values are checked against integration error. The older $(9, 6)$ basis is not used for the final figures: it shifts the PM reference peak and the stronger-G AP curve appreciably. Appendix Figure 15 displays the actual discrepancy separately for each named parameter setting and each pair. The $G/\omega_m = 0.16$ case is the most sensitive in the basis comparisons, with maximum differences 1.95×10^{-8} (AP), 9.89×10^{-9} (AM), and 4.36×10^{-5} (PM); all remain below the prescribed 10^{-4} target. For the time-step comparison, the greatest AP and PM discrepancies also occur at $G/\omega_m = 0.16$, whereas the greatest AM discrepancy occurs at $\Omega_Z/\omega_m = 0.80$. These comparisons establish finite-grid consistency of the displayed results, not an exact solution of the unbounded model.

We report sampled maxima on the output grid, not continuously optimized extrema. Time averages are trapezoidal approximations to

$$\overline{\mathcal{N}}_{X:Y} = \frac{1}{30} \int_0^{30} \mathcal{N}_{X:Y}(\tau)\, d\tau. \tag{24}$$

The output interval is specified independently of the integration step, and peak locations remain

grid- and window-dependent. Relative initial phase is additionally scanned at 17 uniformly spaced values over $0 \leq \phi \leq 2\pi$ with all Hamiltonian parameters, coherent amplitudes and numerical cutoffs otherwise fixed; the new phase-scan figure reports atomic entropy only, not uncalculated phase-dependent pair negativities. Numerical data include all three pair negativities for every scan. The pairwise-negativity data were generated with the supplied Python implementation and cross-checked with a MATLAB solver. The newly added atomic observables were explicitly recalculated by the included independent Python propagation script; the MATLAB plotting driver does not generate these new panels.

4 Results and Discussion

4.1 Comparing dynamical traces

We characterize each negativity trace by its largest value on the 1201-point output grid, the time of that value, and its trapezoidal time average. These quantities answer different questions. A high peak need not last, while a relatively modest trace can dominate the average if it remains elevated. The selected window, $0 \leq \tau \leq 30$, and the sampling resolution matter to these statistics. In a closed system, none of them should be called a dissipative entanglement lifetime.

Except for the initial-phase scan, parameter comparisons use the same product-state preparation and change one model parameter at a time. We abbreviate atom, effective plasmon mode, and mechanics by A, P, and M. All three pair negativities are evaluated from the corresponding reductions of the propagated state. The heat maps, running means, and peak-time charts are calculated from the stored trajectories on the same time grid; they do not represent additional dynamical models.

4.2 Reference pairwise dynamics

The three pairs do not build entanglement on the same schedule (Figure 3). Although every negativity starts at zero for the product initial state, the PM pair reaches its largest sampled value, 0.263, already at $\tau = 3.35$. The AM maximum, 0.092, occurs at $\tau = 10.075$, and AP reaches 0.466 at $\tau = 17.75$. The AP peak is close to the qubit–boson bound 1/2, but this numerical proximity does not identify a Bell state or a particular two-dimensional subspace of the plasmon mode. Over the complete interval, the mean negativities are 0.2484 (AP), 0.0353 (AM), and 0.1514 (PM). The early PM maximum is compatible with number-conditioned mechanical displacements that begin as soon as the coherent mode evolves. AM correlations arise by mediation and are smaller in this setting. Their distinct timing is evidence for a changing pattern of pair correlations, not for a conserved quantity being transferred from one pair to another. The three values cannot be added to obtain a total entanglement.

4.3 Atomic excitation, entropy, and purity

Population exchange offers an independent diagnostic of the same evolution. Initially $P_e = P_g = 0.5$ and $\langle a^\dagger a \rangle = |\alpha|^2 = 1.69$, so $\langle Q \rangle = 2.19$ (Figure 4). As the atomic excitation changes, the mode occupation compensates: the observed spread in $\langle Q \rangle$ is 2.66×10^{-11} over the plotted interval. This agrees with the exact excitation constraint, despite the time-dependent exchange coefficient. Inver-

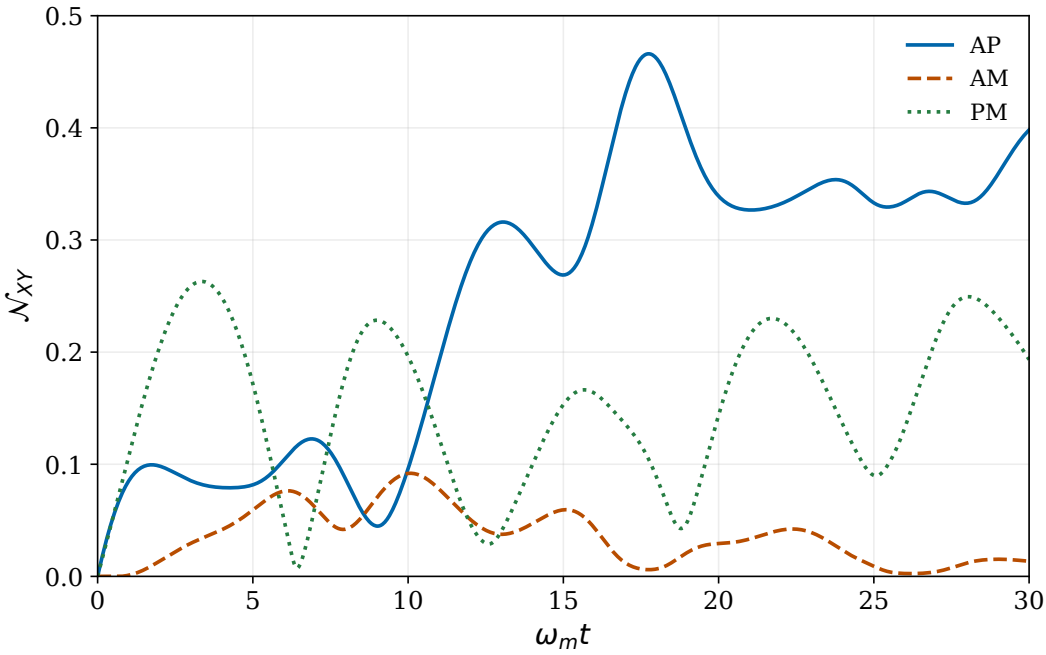


Figure 3: Reference AP, AM, and PM negativities with the parameters in Table 1. AP denotes atom–mode, AM atom–mechanics, and PM mode–mechanics. All curves use the same converged-basis protocol.

sion describes the population imbalance, but not the off-diagonal coherence needed to characterize entanglement.

Atomic entropy and purity complement the pair negativities without replacing them. At the reference setting, S_A reaches 0.9463 bits and has mean 0.4678 bits; the minimum purity is 0.5368 (Figure 5). Because the atom is a qubit, both diagnostics are functions of the eigenvalues of the same reduced state. Their oscillations reflect periods when the atom becomes more mixed and subsequently regains purity under global unitary evolution. Neither curve distinguishes which of the other two subsystems is most strongly entangled with the atom: S_A refers to $A : (PM)$ as a whole.

In Figure 6, increasing g/ω_m through $0.15, 0.25, 0.35$ increases the window-averaged atomic entropy from 0.3479 through 0.4678 to 0.5676 bits. Changing G/ω_m through $0, 0.08, 0.16$ yields means $0.4090, 0.4678, 0.6113$ bits. Yet Figure 8 shows that the AM negativity mean decreases as g grows, confirming that the entanglement across $A : (PM)$ need not follow the entanglement within $A : M$. In the strongest mechanical-coupling case, the independent atomic-entropy propagation changes by at most 4.11×10^{-9} when the bosonic basis is enlarged from $(19, 28)$ to $(21, 32)$; changing the RK4 step from 0.0125 to 0.00625 changes it by at most 5.69×10^{-10}. These are empirical comparisons for this diagnostic, distinct from the archived negativity convergence tests.

4.4 Sensitivity to the initial atomic relative phase

The parameter ϕ in Eq. 7 is a relative preparation phase, not a physically irrelevant global phase. The coherent plasmon amplitude is fixed at the real value $\alpha = 1.30$; changing ϕ therefore changes the phase relation between the initial atomic coherence and the mode. We evolved 17 equally spaced phase choices between 0 and 2π, retaining the same Hamiltonian and calculating ρ_A from

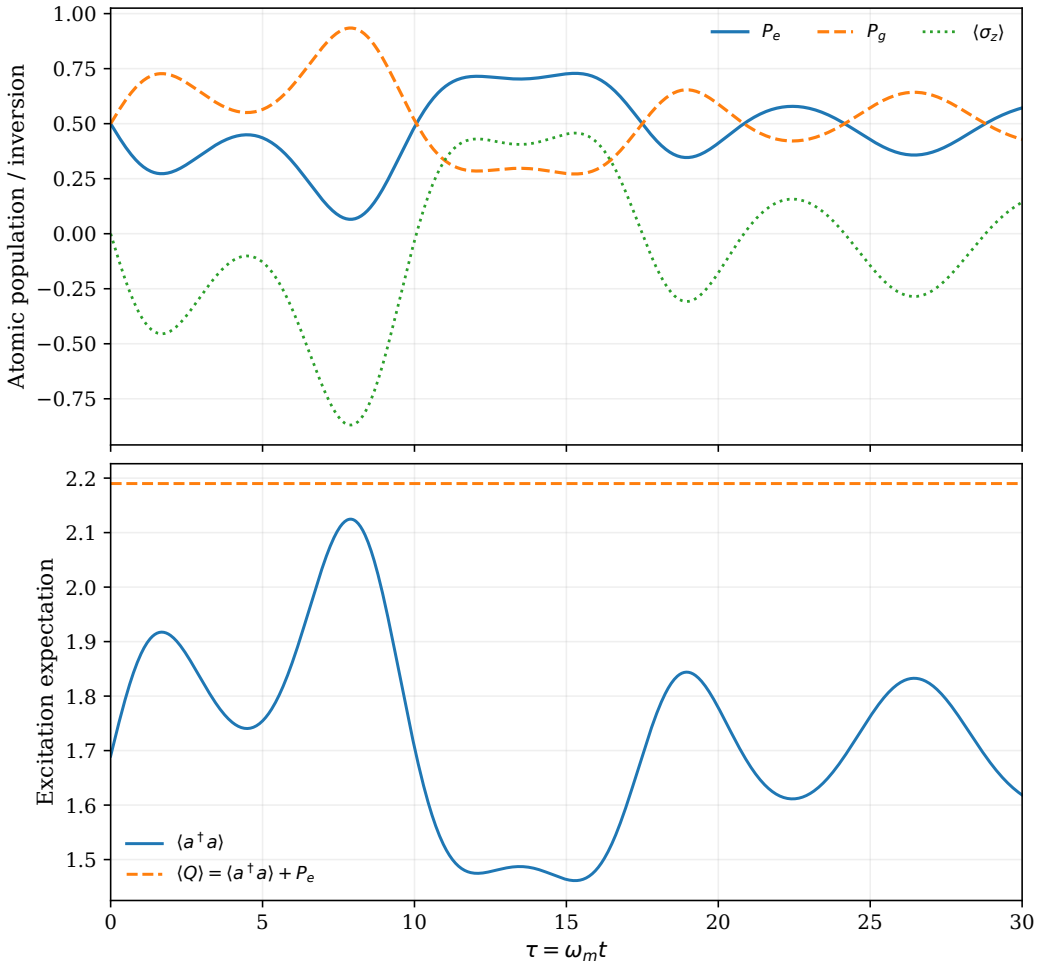


Figure 4: Pure-state propagation at the reference parameters: (a) excited and ground atomic populations and inversion; (b) bosonic population and conserved joint excitation $\langle Q\rangle$. Conservation is visible despite the explicitly time-dependent exchange.

each state trajectory. This isolates a preparation effect from the coupling and detuning sweeps.

Figure 7 shows both the entropy trajectories for selected preparations and the dependence of their sampled peaks and window means on ϕ. The reference $\phi = \pi/4$ gives a mean of 0.4678 bits and peak of 0.9463 bits. For $\phi = 0$, the peak is smaller (0.8206 bits), but the mean is larger (0.5506 bits). Of the 17 sampled choices, $7\pi/8$ has the smallest mean (0.4456 bits), whereas $13\pi/8$ has the largest (0.7017 bits). These are grid values, not continuous-phase optima. The result establishes sensitivity of atomic mixing to preparation; it does not measure loss or decoherence.

Table 3: Directly computed atomic entropy for selected initial phases. All other inputs match Table 1; peaks and means are over $0 \leq \tau \leq 30$.

Initial phase	Sampled maximum (bits)	Time-window mean (bits)
0	0.8206	0.5506
$\pi/4$ (reference)	0.9463	0.4678
$\pi/2$	0.9391	0.4669
π	0.7804	0.4651
$13\pi/8$	0.9942	0.7017

The reference phase trajectory obtained from the phase sweep agrees at every recorded time

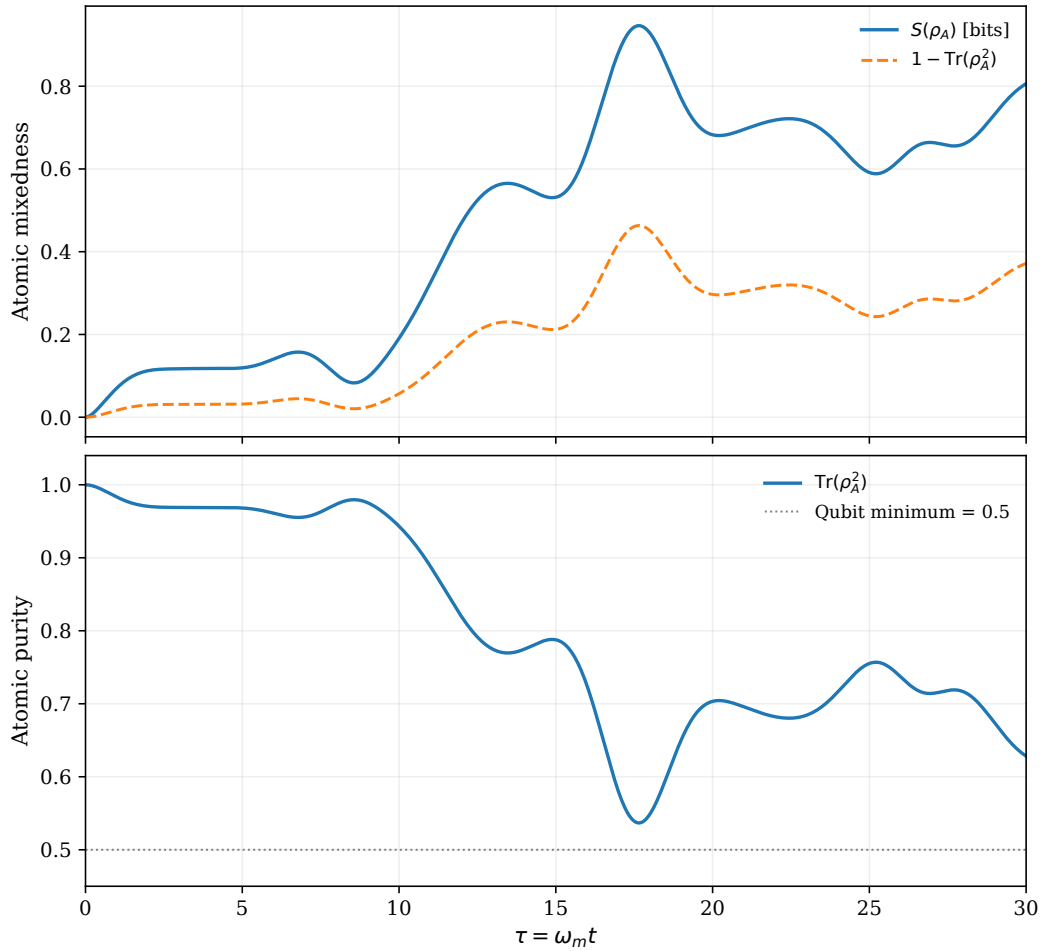


Figure 5: Atomic reduced-state diagnostics: (a) von Neumann entropy S_A in bits and linear entropy $1 - \mathrm{Tr}\rho_A^2$; (b) atomic purity. These characterize $A : (PM)$ for a globally pure state; they do not directly quantify AP or AM mixed-state entanglement.

with the reference atomic-entropy trajectory (maximum recorded absolute difference below machine output precision). The expected excitation $\langle Q \rangle$ remains constant across the phases, with numerical spreads of order 10^{-11}. This check adds one initial-state control to the existing coupling and offset scans, not evidence that the relative phase improves all three reduced pairs. In particular, pairwise phase dependence cannot be claimed from these atomic marginal calculations alone.

4.5 Atom–mode exchange strength

The direct-exchange sweep gives a straightforward AP trend but a less straightforward three-pair response. For $g/\omega_m = 0.15, 0.25, 0.35$, the AP maxima are 0.399, 0.466, and 0.471; the corresponding means are 0.182, 0.248, and 0.313. Over these sampled values, strengthening the exchange raises the AP mean consistently. The increase in the maximum is smaller between the two higher couplings, illustrating that the peak and average need not respond with the same sensitivity.

Figure 8 plots AP, AM, and PM for the same three exchange strengths. As g/ω_m rises from 0.15 to 0.35, the AM time-average decreases from 0.0550 to 0.0260, while the PM time-average increases from 0.1304 to 0.1661. The AP time-average, by contrast, increases from 0.1822 to 0.2886. Thus the selected scan supports stronger sustained direct atom–mode correlations but not an enhancement of all three reduced-pair negativities at once. The AM sampled peak also

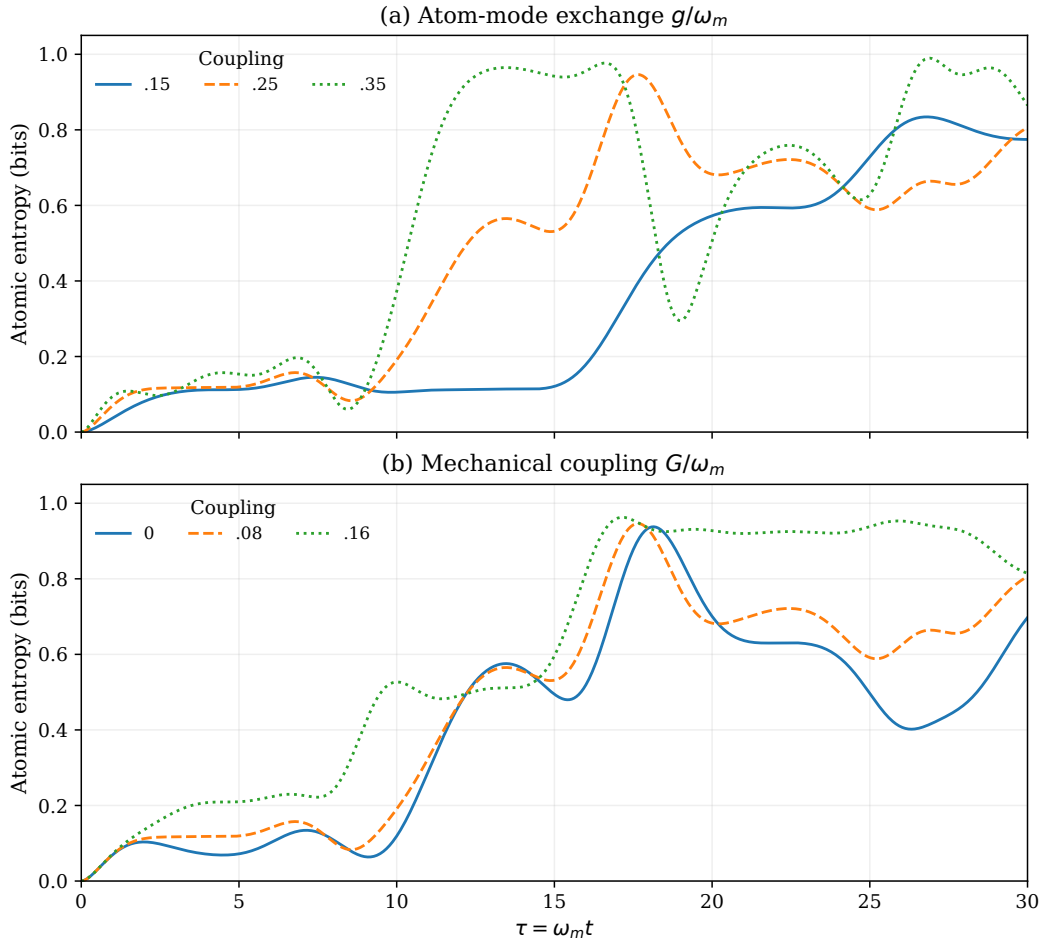


Figure 6: Atomic von Neumann entropy under independent control sweeps: (a) exchange strength g/ω_m; (b) mechanical coupling G/ω_m. The increased atomic entropy is not a claim that all pairwise negativities increase. Each curve was obtained from propagated amplitudes, not reconstructed from negativity.

decreases mildly, from 0.1012 to 0.0891, illustrating that direct exchange and indirect mechanical entanglement are not optimized by the same parameter choice.

4.6 Mechanical coupling and the three reduced pairs

Figure 9 retains AP, AM, and PM rather than AP alone. For $G/\omega_m = 0, 0.08, 0.16$, the AP sampled peaks are 0.478, 0.466, 0.443 and its means are 0.26, 0.248, 0.251. The peak decreases across the tested values, whereas the average is not strictly monotonic. At zero mechanical coupling, AM and PM vanish up to the monitored numerical residual because the mechanics factorizes exactly. At $G/\omega_m = 0.16$, AM and PM reach approximately 0.138 and 0.595. Increasing G does more than suppress a direct atom–mode peak. It gives the oscillator a stronger number-conditioned displacement and allows both pairs involving mechanics to acquire larger correlations. This is a comparison of separate negativities, not conservation or transfer of a fixed entanglement budget. Because the mechanical state moves farther in phase space as G grows [Eq. 12], we checked the oscillator cutoff for each curve. That check matters quantitatively: the old small-basis AP peak of 0.4461 at $G/\omega_m = 0.16$ is replaced by approximately 0.443 on the larger basis.

The finite-window means show where the additional mechanical coupling matters most. As G/ω_m increases from 0 to 0.16, the PM mean rises from zero to 0.3293 and the AM mean from

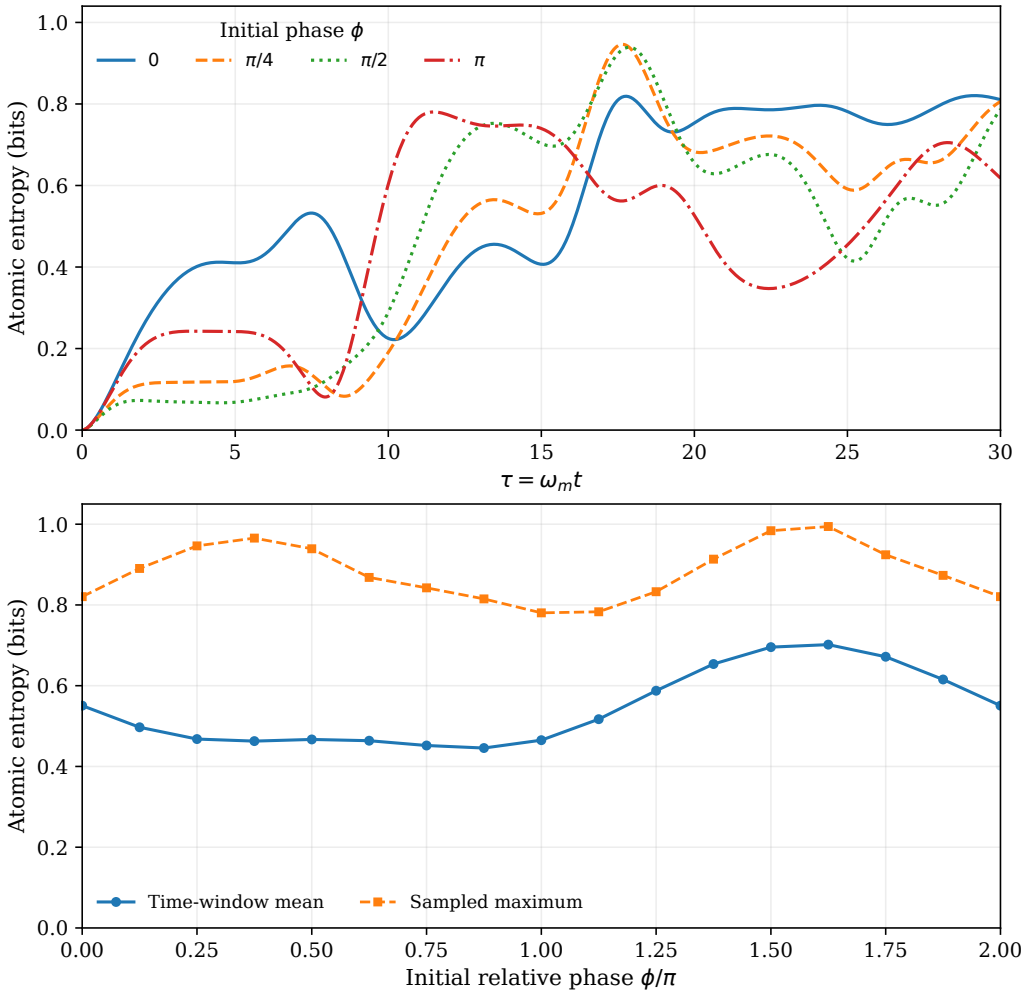


Figure 7: Initial-phase response from state-vector propagation. (a) Atomic von Neumann entropy for four selected relative phases at unchanged model parameters, with the bosonic coherent amplitude real and positive; (b) sampled entropy maxima and full-window entropy means for 17 phases from 0 to 2π. This is an $A{:}(PM)$ diagnostic, not a phase scan of the three pair negativities.

zero to 0.0578. Meanwhile, the AP mean changes only from 0.2597 to 0.2514. Thus the substantial new correlations involve the oscillator, even though AP remains strongly entangled. A discussion restricted to the AP peak would obscure this contrast.

To separate early transients from long observation windows, define the running average

$$\overline{\mathcal{N}}_{X:Y}(0,T) = \frac{1}{T}\int_0^T \mathcal{N}_{X:Y}(\tau)\,d\tau, \qquad 0 < T \leq 30. \tag{25}$$

Figure 10 evaluates this expression using the same time-grid data, so its values at $T = 30$ reproduce the reported full-window means. The running curves emphasize that conclusions based on a short early interval need not persist when the observation window is lengthened; in particular, the PM contribution at larger G remains substantially higher even after averaging over the entire plotted interval.

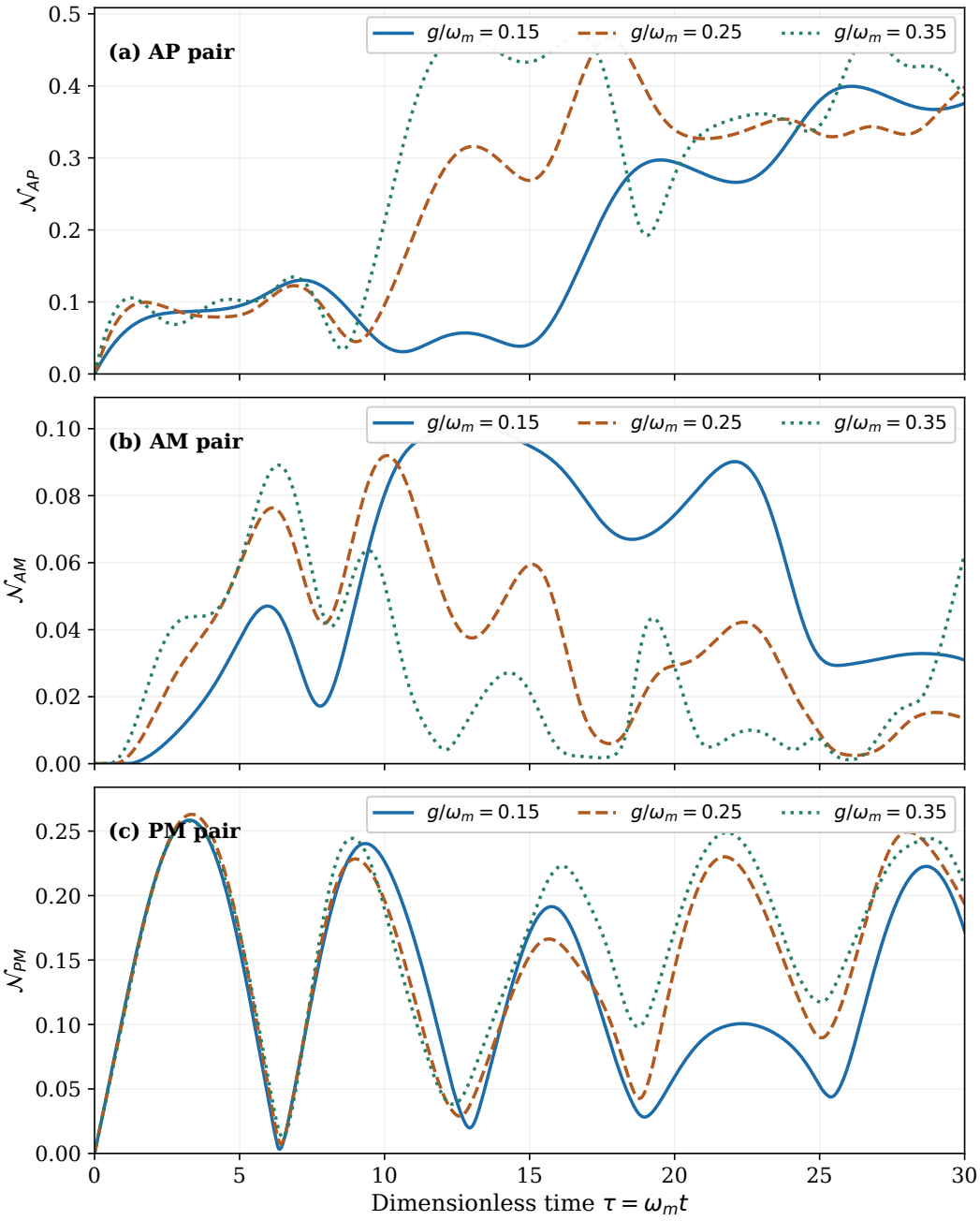


Figure 8: Complete exchange-strength scan for (a) atom–mode, (b) atom–mechanics, and (c) mode–mechanics negativity. Increasing exchange enhances the AP window average but decreases the AM window average for these settings. Different ordinate scales are used to expose each pair.

4.7 Transition-offset scan

With $\Delta_a = \Delta_p = 0$, changing Ω_Z/ω_m from 0 to 0.30 to 0.80 changes the effective offset by the same amounts (Figure 11). The AP sampled maxima are 0.315, 0.466, and 0.428. The intermediate setting therefore gives the highest sampled AP peak of the three, but not necessarily the strongest sustained AP entanglement. The offset changes the phases accumulated during atom–mode exchange; it is not an independent magnetic response of the plasmon or mechanics.

A simple monotonic resonance picture is not enough to explain these curves. Occupation-dependent displacements shift different mode sectors, while the periodic exchange adds further time scales. Their combined phases can enhance or suppress a given transient. The plots establish

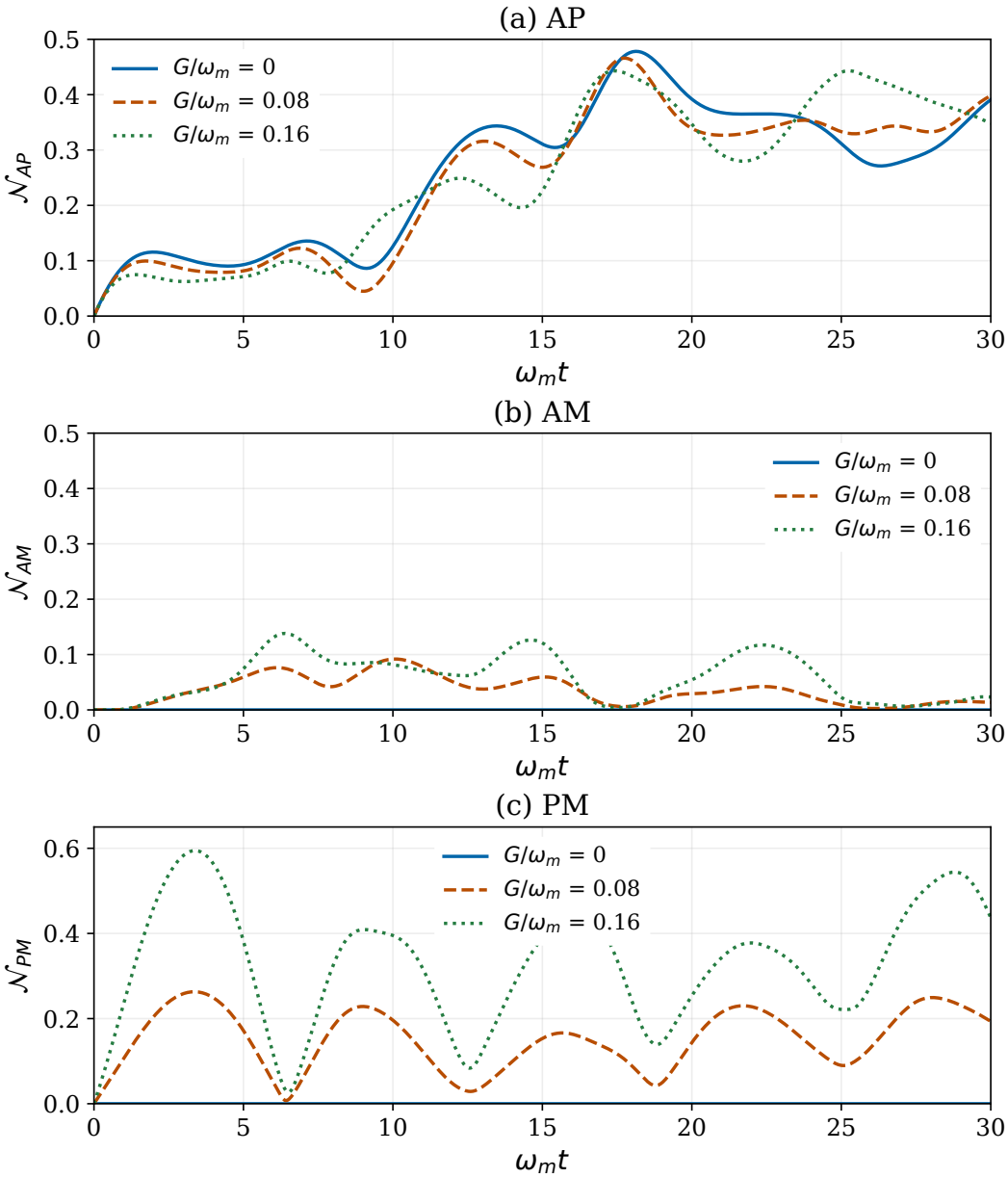


Figure 9: Mechanical-coupling scans for (a) AP, (b) AM, and (c) PM. The PM vertical scale differs because its negativity is not bounded by 1/2. The $G = 0$ mechanics factorizes; tiny integrator residuals are not interpreted as physical entanglement.

the net parameter dependence, but not which dressed-state or Floquet pathways dominate it; that would require a separate spectral calculation.

In the full three-pair view, the other pairs respond differently from the AP peak pattern. As Ω_Z/ω_m increases through $0, 0.30, 0.80$, the AP means are $0.1318, 0.2484, 0.2717$: the mean continues to rise over these three settings even though the sampled peak is largest at the intermediate offset. Conversely, the AM means decline from 0.0478 to 0.0156, and the PM means decline from 0.1705 to 0.1361. This difference between a maximum and an average should be made explicit whenever a detuning is described as favorable. A peak at the endpoint $\tau = 30$ is not proof that an intrinsic global maximum has been reached.

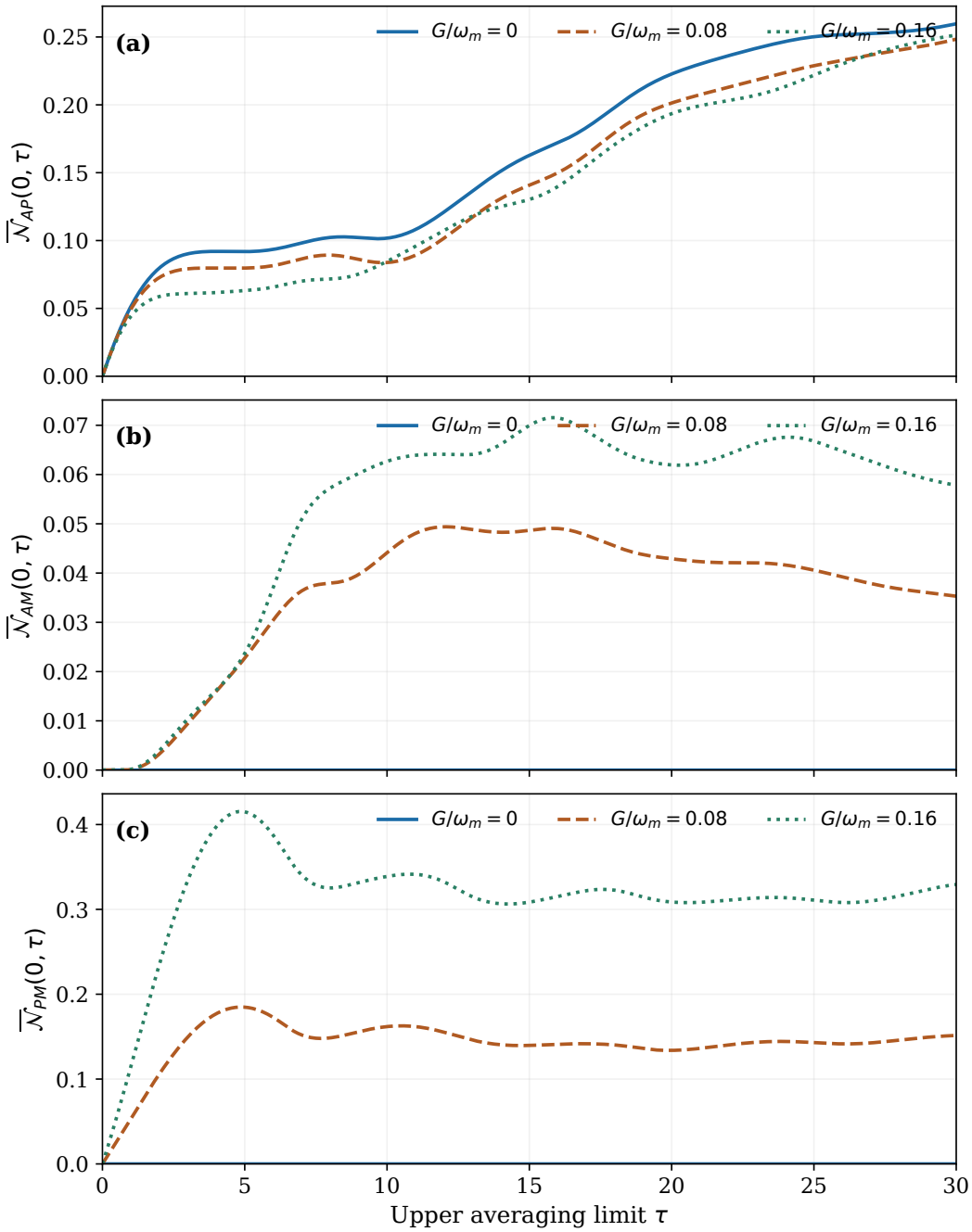


Figure 10: Running mean negativities as functions of the upper integration limit T for three mechanical couplings: (a) AP, (b) AM, and (c) PM. These are trapezoidal integrals of the already validated negativity trajectories, not new dynamical simulations. The first time point is assigned zero for display; Eq. 25 applies for $T > 0$.

4.8 Prescribed atomic motion

A stationary exchange profile and a moving one cannot be ranked from one peak alone. At $\nu_{\mathrm{mot}}/\omega_m = 0, 0.35, 0.70$, the AP sampled maxima are 0.44, 0.466, and 0.435, whereas the means are 0.311, 0.248, and 0.235. The reference modulation produces the highest peak; the stationary profile produces the highest AP mean. This comparison concerns the specified cosine couplings, not a search for the optimal experimental velocity.

When the coupling changes sign across a standing-wave lobe, it also changes the relative phase

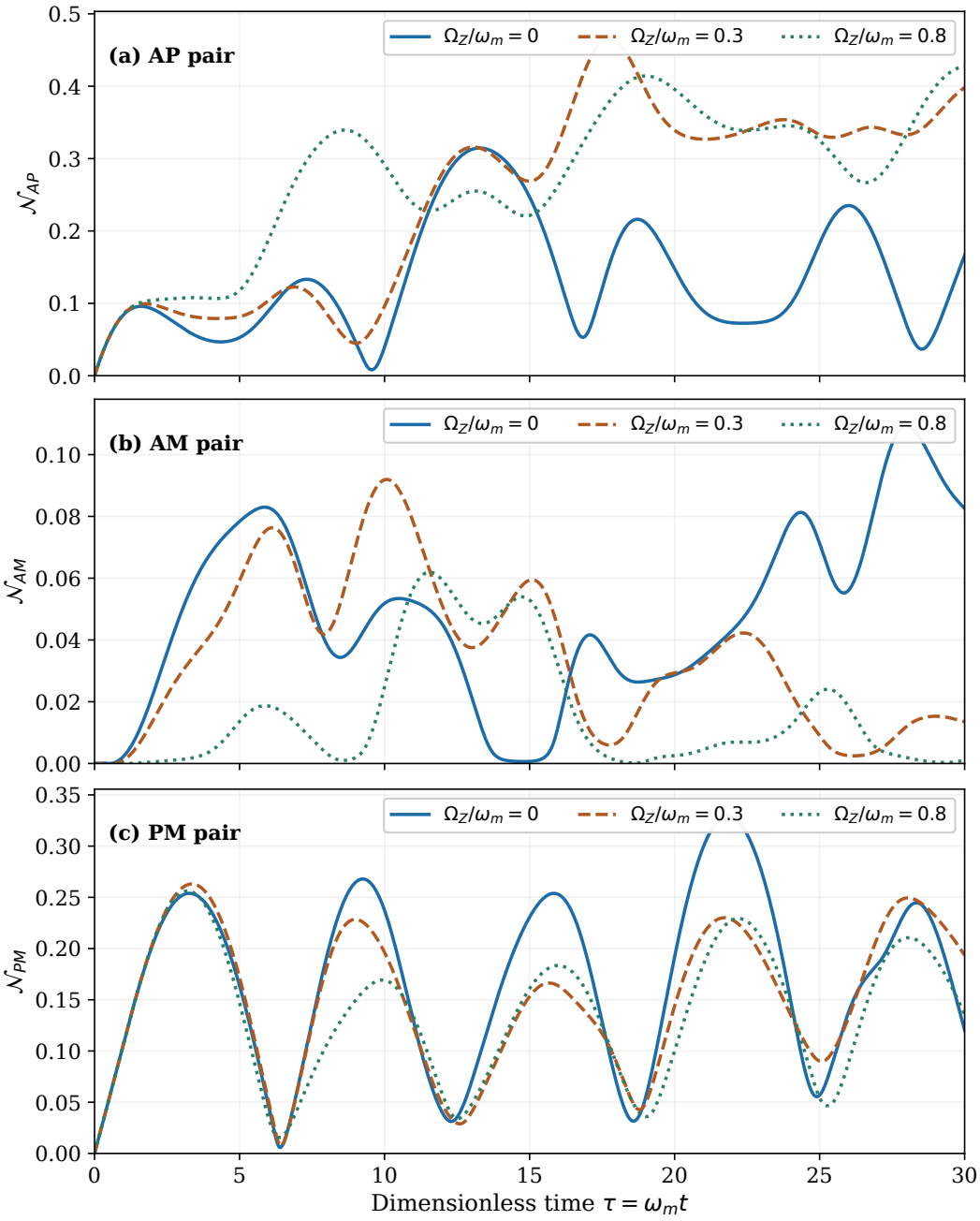


Figure 11: All three reduced-pair negativities under the Zeeman-type offset scan: (a) AP, (b) AM, and (c) PM. The three curves in each panel differ only through the effective atomic offset in Eq. 5. The AP peak ranking is not the same as the ranking of the AP time averages.

accumulated by different excitation pathways. Replacing the profile with a weaker constant coupling would generally miss this effect. The resulting dips and revivals occur in unitary dynamics and should not be described as irreversible decoherence.

Figure 12 gives the full pairwise response to these modulation frequencies. The stationary setting has a mean PM negativity of 0.2574, considerably above 0.1514 at the reference modulation and 0.1310 at the faster modulation. Its mean AP negativity is also highest, at 0.3113 compared with 0.2484 and 0.2349. Yet the reference motion frequency has the largest AP sampled peak, 0.466. A useful interpretation is therefore objective-dependent: modulation can change the timing of exceptionally large entanglement while lowering the correlation present on average. This should

not be described as motion-induced decoherence, since there is no dissipative or fluctuating atomic velocity in the model.

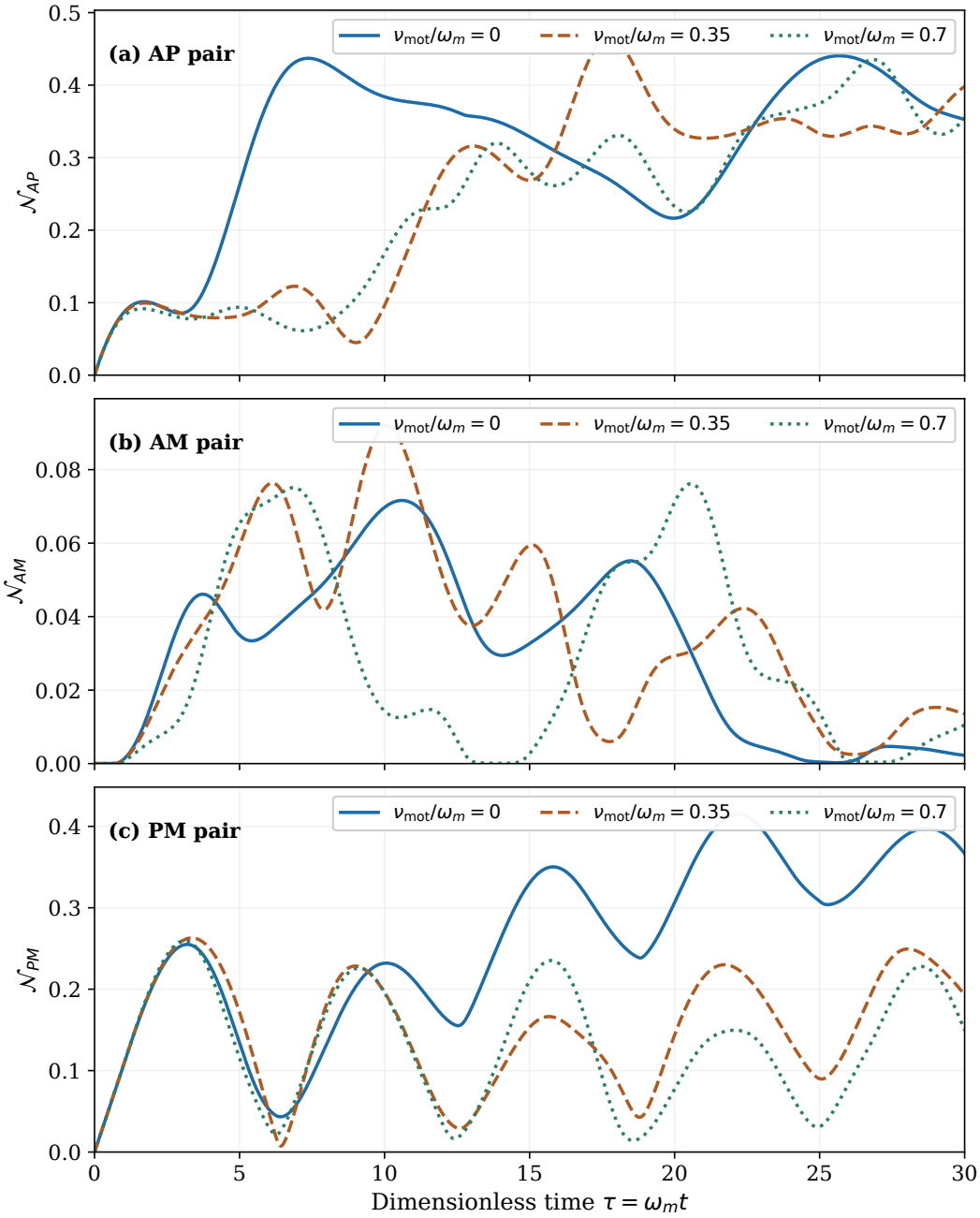


Figure 12: Complete motion-frequency scan for (a) AP, (b) AM, and (c) PM negativity. The atom follows the prescribed envelopes of Figure 2; no motional state, recoil, or spatial intensity envelope is evolved.

4.9 One effective atomic offset

The rotating-frame dynamics depend on the atomic and plasmon frequencies through $\delta = \Delta_a + \Omega_Z - \Delta_p$, so a Zeeman-type shift and bare atomic detuning are not separate controls in this Hamiltonian. For example, with $\Omega_Z/\omega_m = 0.30$ and $\Delta_p = 0$, choosing $\Delta_a/\omega_m = +0.50$ yields $\delta/\omega_m = 0.80$: the resulting trajectory is identical to the zero-bare-detuning curve at $\Omega_Z/\omega_m = 0.80$. The choice $\Delta_a/\omega_m = -0.50$ instead gives $\delta/\omega_m = -0.20$, with AP peak 0.467 and mean 0.2755. We show

this negative-offset case only once in the distinct-setting summary. The model contains no direct magnetic modification of the plasmon spectrum or mechanical force.

4.10 Cross-scan comparison of entanglement objectives

Figure 13 places the two most common optimization criteria side by side. It compares the sampled peak and finite-window mean for ten distinct settings; duplicate detuning labels and repeated baselines have been removed. Within a given pair, the color pattern makes it easy to see which control settings favor brief maxima and which favor sustained correlations. The absolute values across AP, AM, and PM are not on a common entanglement scale, so comparisons should be made mainly within each pair's column.

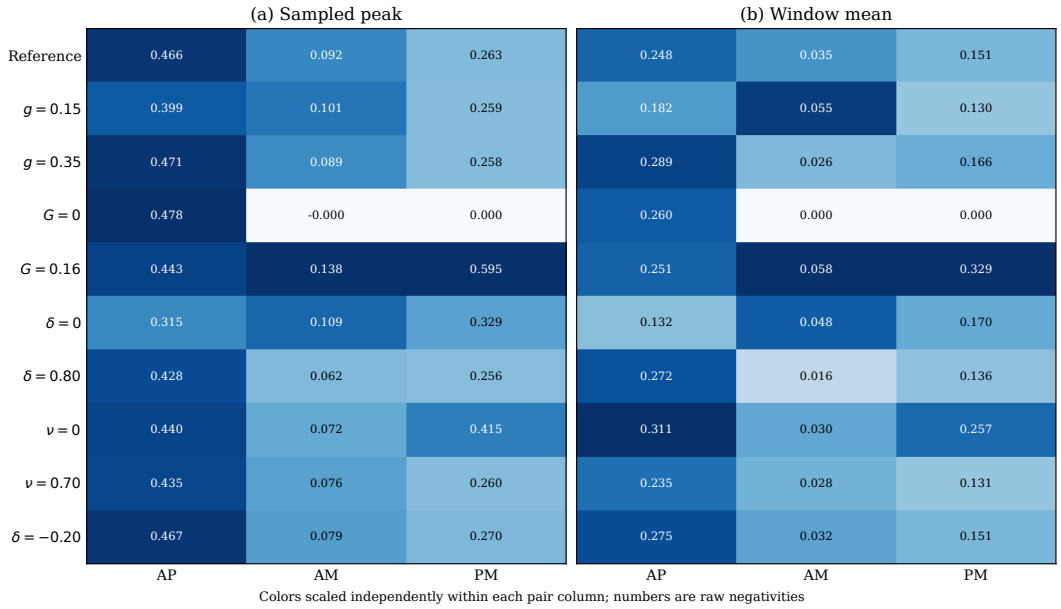


Figure 13: Sampled maxima and full-window time averages for ten physically distinct settings. Colors are normalized separately for each pair column only to facilitate vertical scanning; every cell displays the original raw negativity. Labels g, G, δ, ν are expressed relative to ω_m. Identical effective-offset and baseline duplicates are excluded.

For $G/\omega_m = 0.16$, the largest sampled PM negativity is 0.5945, while the AP and AM peaks are 0.4432 and 0.1382. A PM value above 1/2 is allowed: both components are bosonic, and their accessible entanglement scale differs from that of a qubit–boson pair. The AP peak is lower than its reference value 0.4660, yet the AM peak is higher. These responses point to different pairwise sensitivities, not a one-for-one conversion between them. The exchange scan provides another counterexample to a single "entanglement enhancement" label: increasing g/ω_m from 0.15 to 0.35 raises the AP mean while lowering the AM mean.

The occurrence times of the sampled maxima provide another useful characterization (Figure 14). For the reference parameters, PM peaks at $\tau = 3.35$, AM at 10.075, and AP at 17.75. Under the strongest mechanical coupling the three peak times are approximately 25.25, 6.40, and 3.375 for AP, AM, and PM. No general ordering follows: the peak times depend on the Hamiltonian parameters and can fall at the observation boundary. For $G = 0$, both mechanical pair negativities vanish, so assigning them a physically meaningful maximization time would be misleading and those symbols are omitted.

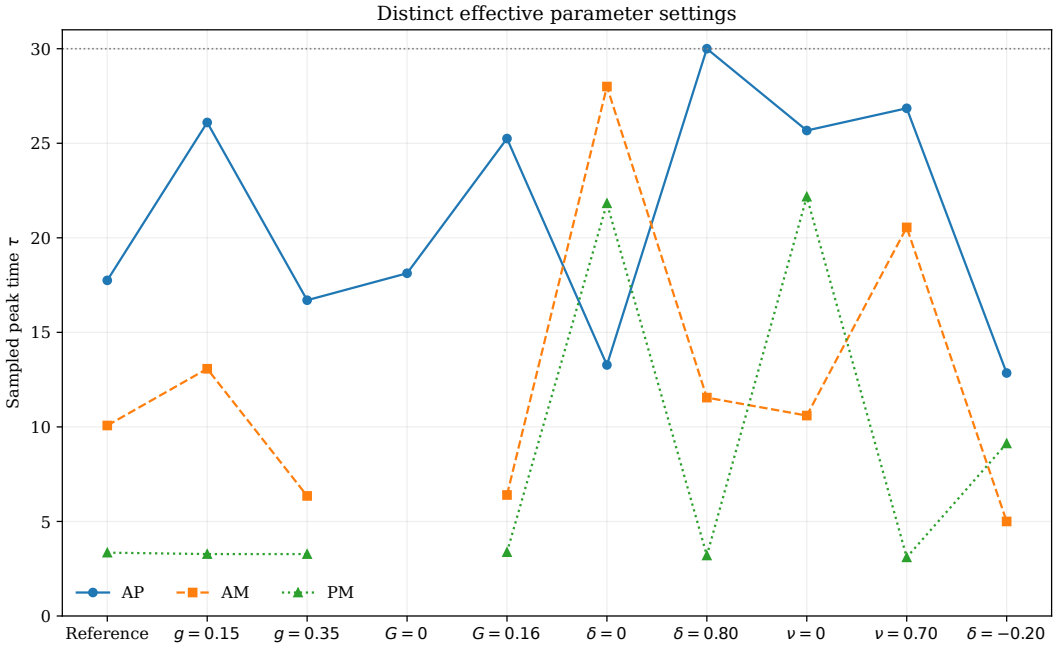


Figure 14: Times at which the sampled AP, AM, and PM negativity maxima occur for ten non-duplicated physical settings within the common window. The horizontal dotted line indicates the final observation time. A point at that boundary is a window-limited maximum, not evidence of a global peak. Vanishing mechanical entanglement for $G = 0$ has no meaningful peak time and is omitted.

4.11 Numerical provenance and reproducibility

The numerical results have two sources. The negativity sweeps, running means, and distinct-setting heat maps are evaluated from stored full-grid AP, AM, and PM trajectories at $\tau = 0, 0.025, \ldots, 30$, without interpolation beyond that window. Atomic populations, entropy, and purity were obtained by state-vector propagation followed by direct reduction of the atomic density matrix; the initial-phase sweep and strong-G third-basis comparison use the same propagation framework. The supplement includes the trajectory data, numerical settings, scripts, and exported MAT/CSV summaries. Keeping the source of each plotted quantity explicit allows its calculation to be repeated and avoids presenting post-processed arrays as independent simulation runs.

The simulations are reproducible statements about a finite, closed Hamiltonian model. Repeating them does not supply missing environmental physics or a microscopic calculation of the effective couplings. The plots do not include uncertainty in g, G, the imposed modulation, or reservoir-induced damping, so their numerical stability should not be confused with robustness to those effects.

4.12 Physical scope and limitations

To relate the effective mode to a particular nanocavity or plasma structure, its frequency and field distribution would have to be derived from that system. The present model includes no many-mode spectrum, microscopic kinetic response, or density-dependent calculation. The displacement coupling G is likewise a phenomenological parameter until a mode geometry and mechanical coordinate are specified. A device-level comparison would require the emitter transition and dipole, field overlap, mode separation, linewidths, bath temperatures, and a realizable atomic trajectory.

Those parameters must be compatible with the rotating-wave approximation, isolation of one

mode, and the low-occupation displacement expansion. In addition, loss must remain negligible over the modeled interval $30/\omega_m$ if the unitary curves are to approximate an experiment. Plasmon damping, mechanical heating, and thermal or non-Markovian material response have not been propagated here. Entanglement survival in an experimental platform is therefore an open calculation, not a conclusion of the present parameter scan.

5 Conclusion

The three reduced pairs of the atom–plasmon–mechanics model respond quite differently, despite evolving under the same global pure state. In the reference run, the largest sampled negativities are 0.466 for AP, 0.0920 for AM, and 0.263 for PM. The PM maximum precedes the AM and AP maxima. This timing, together with the coupling scans, is consistent with direct atom–mode exchange and occupation-dependent mechanical displacement producing distinct paths to pairwise correlations.

The clearest parameter dependence appears in the mechanical sector. Increasing G strongly increases the mean AM and PM negativities over the tested values, while leaving the AP mean comparatively similar. Increasing g raises the mean AP negativity but reduces the mean AM negativity. A prescribed cosine modulation can also yield a larger isolated AP maximum than stationary coupling while giving a lower AP average. Thus a statement that a parameter "enhances entanglement" is incomplete unless it identifies the pair, time window, and statistic being compared. The curves do not imply that the three negativities sum to a conserved quantity.

Atomic entropy adds a different observation: the atom may be entangled with the rest of the system without that entanglement belonging to a specific reduced pair. The mean atomic entropy changes from 0.4456 to 0.7017 bits across the 17 sampled initial phases, even though the Hamiltonian is unchanged. This phase sensitivity is a preparation effect. It also reinforces the distinction between a brief maximum and the average over $0 \leq \omega_m t \leq 30$. Truncation and integration-step tests support the reported finite-time comparisons, including a targeted third-basis check at the strongest mechanical coupling, but they do not constitute an exact error bound.

The findings apply to a unitary, single-effective-mode Hamiltonian. Its detuning and Zeeman-type shift enter through the same offset, and it contains neither microscopic plasma response nor environmental loss. Establishing whether the observed correlations persist in a specific plasmonic implementation will require a mode-resolved coupling model and open-system calculations with damping and thermal occupation. Within its stated scope, the present analysis demonstrates why the three pair negativities and the atom–rest entropy should be evaluated separately.

A Detailed convergence diagnostics

The archived per-setting comparison is displayed in Figure 15. The largest measured deviations are summarized in Table 2. Reference settings appear under more than one parameter-scan label in the archived check only to retain full provenance; they do not constitute independent Hamiltonians. For atomic entropy and inversion, the new script `add_physical_diagnostics.py` repeats direct propagation at $(21, 32)$ and at half the production integration step for the reference and strongest mechanical-coupling settings. These checks estimate numerical sensitivity on the tested grid, not a provable continuum error bound.

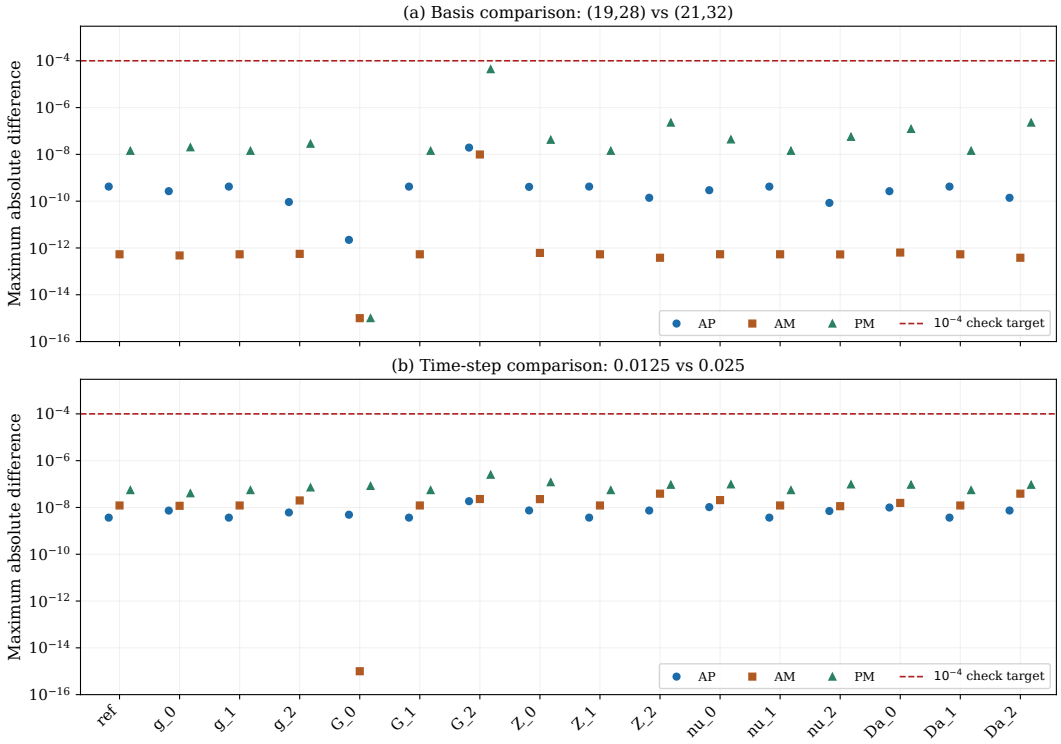


Figure 15: Maximum pointwise absolute differences of the AP, AM, and PM negativity curves over $0 \leq \tau \leq 30$ for (a) the enlarged-basis and (b) the halved-integration-step comparisons. Each dot represents a labelled scan case; repeated reference settings are deliberately retained. The dashed line marks the numerical acceptance target, not a physical entanglement threshold. Values displayed at the lower floor indicate differences below plotting resolution.

B Strong-coupling third-basis check and numerical provenance

The full-grid comparison in Table 2 uses 19×28 and 21×32 bosonic bases over all 1201 output times. Because the strongest mechanical coupling $G/\omega_m = 0.16$ was the most cutoff-sensitive case, we performed an additional targeted run at 23×36 using the same fourth-order propagator and time step 0.0125. This added check outputs 61 values at $\tau = 0, 0.5, \ldots, 30$; it does *not* replace the earlier all-time comparison and should not be confused with it.

Table 4: Maximum pointwise absolute negativity discrepancies for the strong-G control, each over the same 61 sampled times. Edge populations refer to the 23×36 run. These are empirical finite-basis comparisons.

Bosonic-basis comparison	AP	AM	PM
$(19, 28)$ vs $(21, 32)$	1.71×10^{-8}	8.41×10^{-9}	4.17×10^{-5}
$(21, 32)$ vs $(23, 36)$	1.30×10^{-9}	1.22×10^{-9}	1.47×10^{-5}

For $G/\omega_m = 0.16$ at 23×36, the largest sampled plasma and mechanical boundary occupations are 1.12×10^{-16} and 5.60×10^{-13}. The third-basis PM discrepancies are smaller than those at the preceding basis enlargement on the same sparse comparison grid, although this observation alone does not prove monotonic convergence or bound the unbounded-basis error. Figure 16 shows the pairwise differences directly. Because the figure uses a coarse output subset, its maxima must not be reported as full-grid maxima.

The numerical package separates archived 1201-point pair-negativity trajectories, independently propagated atomic-observable trajectories, newly computed phase controls, and the

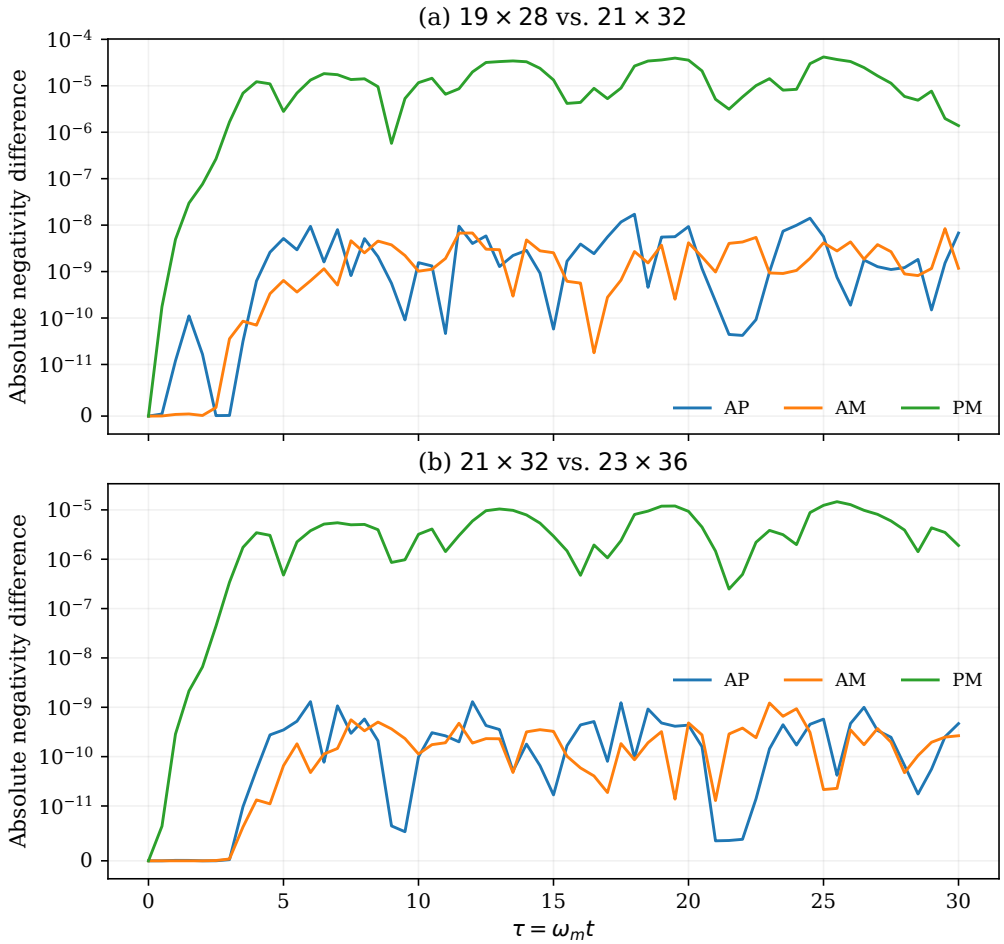


Figure 16: Additional targeted strong-mechanical-coupling ($G/\omega_m = 0.16$) check at 61 common output times: (a) 19×28 versus 21×32 and (b) 21×32 versus 23×36. Absolute errors for all three pairs are plotted on a symmetric-logarithmic ordinate for legibility. See Table 4 and do not interpret these differences as rigorous error bounds.

third-basis diagnostic. The compressed NumPy arrays (NPZ), cross-checked MATLAB summary file (MAT), CSV reference exports and validation/provenance JSON files are included. Hashes and dimensions are recorded in the manifest, and the executable environment is described in `requirements.txt` and `computing_environment.json`. Supplying code or arrays does not imply that every MATLAB script was rerun in the present environment. The new calculations were executed with the bundled Python scripts; the full existing negativity sweep was *not* rerun for this revision.

Declarations

Ethics approval and consent to participate: Not applicable. This theoretical and numerical study did not involve human participants, human data, or animals.

Consent for publication: Not applicable; no identifiable information relating to human participants is included.

Funding: The authors received no financial support for the research, authorship, or publication of this work.

Competing interests: The authors declare that they have no competing financial or non-financial interests.

Author contributions: S. Jamal Anwar conceived the research, developed the theoretical model, performed the analytical and numerical calculations, prepared the figures, and wrote the original manuscript. S. Abdul Khalek reviewed the mathematical analysis and the manuscript and contributed to critical revisions.

Data availability: No experimental or externally acquired research dataset was used, and no research data have been deposited in a public repository. Numerical output files supporting the figures are retained in the authors' working files and included in the private computational package accompanying this manuscript; this package is not a public data archive.

Code availability: No code has been deposited in a public repository. MATLAB and Python source files for the numerical study and figure preparation are included in the authors' private working ZIP package. The package has not been released publicly.

Acknowledgments: None.

References

[1] A. Einstein, B. Podolsky, and N. Rosen, Can quantum-mechanical description of physical reality be considered complete?, Phys. Rev. **47**, 777–780 (1935). doi:10.1103/physrev.47.777.

[2] E. Schrödinger, Discussion of probability relations between separated systems, Math. Proc. Cambridge Philos. Soc. **31**, 555–563 (1935). doi:10.1017/s0305004100013554.

[3] J. S. Bell, On the Einstein Podolsky Rosen paradox, Physics **1**, 195–200 (1964). doi:10.1103/physicsphysiquefizika.1.195.

[4] R. F. Werner, Quantum states with Einstein–Podolsky–Rosen correlations admitting a hidden-variable model, Phys. Rev. A **40**, 4277–4281 (1989). doi:10.1103/physreva.40.4277.

[5] A. Peres, Separability criterion for density matrices, Phys. Rev. Lett. **77**, 1413–1415 (1996). doi:10.1103/physrevlett.77.1413.

[6] M. Horodecki, P. Horodecki, and R. Horodecki, Separability of mixed states: necessary and sufficient conditions, Phys. Lett. A **223**, 1–8 (1996). doi:10.1016/s0375-9601(96)00706-2.

[7] C. H. Bennett, D. P. DiVincenzo, J. A. Smolin, and W. K. Wootters, Mixed-state entanglement and quantum error correction, Phys. Rev. A **54**, 3824–3851 (1996). doi:10.1103/physreva.54.3824.

[8] W. K. Wootters, Entanglement of formation of an arbitrary state of two qubits, Phys. Rev. Lett. **80**, 2245–2248 (1998). doi:10.1103/physrevlett.80.2245.

[9] G. Vidal and R. F. Werner, Computable measure of entanglement, Phys. Rev. A **65**, 032314 (2002). doi:10.1103/physreva.65.032314.

[10] M. B. Plenio, Logarithmic negativity: a full entanglement monotone that is not convex, Phys. Rev. Lett. **95**, 090503 (2005). doi:10.1103/physrevlett.95.090503.

[11] V. Coffman, J. Kundu, and W. K. Wootters, Distributed entanglement, Phys. Rev. A **61**, 052306 (2000). doi:10.1103/physreva.61.052306.

[12] R. Horodecki, P. Horodecki, M. Horodecki, and K. Horodecki, Quantum entanglement, Rev. Mod. Phys. **81**, 865–942 (2009). doi:10.1103/revmodphys.81.865.

[13] E. T. Jaynes and F. W. Cummings, Comparison of quantum and semiclassical radiation theories with application to the beam maser, Proc. IEEE **51**, 89–109 (1963). doi:10.1109/proc.1963.1664.

[14] J. H. Eberly, N. B. Narozhny, and J. J. Sanchez-Mondragon, Periodic spontaneous collapse and revival in a simple quantum model, Phys. Rev. Lett. **44**, 1323–1326 (1980). doi:10.1103/physrevlett.44.1323.

[15] N. B. Narozhny, J. J. Sanchez-Mondragon, and J. H. Eberly, Coherence versus incoherence: collapse and revival in a simple quantum model, Phys. Rev. A **23**, 236–247 (1981). doi:10.1103/physreva.23.236.

[16] J. Gea-Banacloche, Collapse and revival of the state vector in the Jaynes–Cummings model: an example of state preparation by a quantum apparatus, Phys. Rev. Lett. **65**, 3385–3388 (1990). doi:10.1103/physrevlett.65.3385.

[17] S. J. D. Phoenix and P. L. Knight, Fluctuations and entropy in models of quantum optical resonance, Ann. Phys. **186**, 381–407 (1988). doi:10.1016/0003-4916(88)90006-1.

[18] S. J. D. Phoenix and P. L. Knight, Periodicity, phase, and entropy in models of two-photon resonance, J. Opt. Soc. Am. B **7**, 116–124 (1990). doi:10.1364/JOSAB.7.000116.

[19] E. Boukobza and D. J. Tannor, Entropy exchange and entanglement in the Jaynes–Cummings model, Phys. Rev. A **71**, 063821 (2005). doi:10.1103/physreva.71.063821.

[20] N. I. Cummings and B. L. Hu, Dynamics of atom–field entanglement: towards strong-coupling and non-Markovian regimes, Phys. Rev. A **77**, 053823 (2008). doi:10.1103/physreva.77.053823.

[21] C. K. Law and J. H. Eberly, Arbitrary control of a quantum electromagnetic field, Phys. Rev. Lett. **76**, 1055–1058 (1996). doi:10.1103/physrevlett.76.1055.

[22] E. Altewischer, M. P. van Exter, and J. P. Woerdman, Plasmon-assisted transmission of entangled photons, Nature **418**, 304–306 (2002). doi:10.1038/nature00869.

[23] S. Fasel, F. Robin, E. Moreno, D. Erni, N. Gisin, and H. Zbinden, Energy-time entanglement preservation in plasmon-assisted light transmission, Phys. Rev. Lett. **94**, 110501 (2005). doi:10.1103/physrevlett.94.110501.

[24] A. V. Akimov et al., Generation of single optical plasmons in metallic nanowires coupled to quantum dots, Nature **450**, 402–406 (2007). doi:10.1038/nature06230.

[25] R. Kolesov et al., Wave–particle duality of single surface plasmon polaritons, Nat. Phys. **5**, 470–474 (2009). doi:10.1038/nphys1278.

[26] D. E. Chang, A. S. Sørensen, P. R. Hemmer, and M. D. Lukin, Quantum optics with surface plasmons, Phys. Rev. Lett. **97**, 053002 (2006). doi:10.1103/physrevlett.97.053002.

[27] D. E. Chang, A. S. Sørensen, P. R. Hemmer, and M. D. Lukin, Strong coupling of single emitters to surface plasmons, Phys. Rev. B **76**, 035420 (2007). doi:10.1103/physrevb.76.035420.

[28] A. González-Tudela, D. Martín-Cano, E. Moreno, L. Martín-Moreno, C. Tejedor, and F. J. García-Vidal, Entanglement of two qubits mediated by one-dimensional plasmonic waveguides, Phys. Rev. Lett. **106**, 020501 (2011). doi:10.1103/physrevlett.106.020501.

[29] J. S. Fakonas, H. Lee, Y. A. Kelaita, and H. A. Atwater, Two-plasmon quantum interference, Nat. Photonics **8**, 317–320 (2014). doi:10.1038/nphoton.2014.40.

[30] G. Di Martino et al., Quantum statistics of surface plasmon polaritons in metallic stripe waveguides, Nano Lett. **12**, 2504–2508 (2012). doi:10.1021/nl300671w.

[31] R. W. Heeres, S. N. Dorenbos, B. Koene, G. S. Solomon, L. P. Kouwenhoven, and V. Zwiller, On-chip single plasmon detection, Nano Lett. **10**, 661–664 (2010). doi:10.1021/nl903761t.

[32] M. Asano et al., Distillation of photon entanglement using a plasmonic metamaterial, Sci. Rep. **5**, 18313 (2015). doi:10.1038/srep18313.

[33] L. Piazza et al., Simultaneous observation of the quantization and the interference pattern of a plasmonic near-field, Nat. Commun. **6**, 6407 (2015). doi:10.1038/ncomms7407.

[34] Z. Sun, D. N. Basov, and M. M. Fogler, Graphene as a source of entangled plasmons, Phys. Rev. Research **4**, 023208 (2022). doi:10.1103/physrevresearch.4.023208.

[35] G. Calajó et al., Nonlinear quantum logic with colliding graphene plasmons, Phys. Rev. Research **5**, 013188 (2023). doi:10.1103/physrevresearch.5.013188.

[36] L. Brey and H. A. Fertig, Quantum plasmons in double-layer systems, Phys. Rev. B **109**, 045303 (2024). doi:10.1103/physrevb.109.045303.

[37] K. Qu and N. J. Fisch, Producing entangled photon pairs and quantum squeezed states in plasmas, Phys. Rev. E **110**, 065211 (2024). doi:10.1103/physreve.110.065211.

[38] X.-H. Jiang et al., Quantum teleportation mediated by surface plasmon polariton, Sci. Rep. **10**, 11503 (2020). doi:10.1038/s41598-020-67773-1.

[39] G. Manfredi, How to model quantum plasmas, Fields Inst. Commun. **46**, 263–287 (2005). doi:10.1090/fic/046/10.

[40] F. Haas, A magnetohydrodynamic model for quantum plasmas, Phys. Plasmas **12**, 062117 (2005). doi:10.1063/1.1939947.

[41] M. Marklund and G. Brodin, Dynamics of spin-1/2 quantum plasmas, Phys. Rev. Lett. **98**, 025001 (2007). doi:10.1103/physrevlett.98.025001.

[42] P. K. Shukla and B. Eliasson, Formation and dynamics of dark solitons and vortices in quantum electron plasmas, Phys. Rev. Lett. **96**, 245001 (2006). doi:10.1103/physrevlett.96.245001.

[43] Y. Zhang, Y. Wang, W. Jiang, and W. Li, BCS–BEC crossover of ultracold ions driven by density-dependent short-range interactions in a quantum plasma, Phys. Rev. A **104**, 063312 (2021). doi:10.1103/PhysRevA.104.063312.

[44] A. Dorsel, J. D. McCullen, P. Meystre, E. Vignes, and H. Walther, Optical bistability and mirror confinement induced by radiation pressure, Phys. Rev. Lett. **51**, 1550–1553 (1983). doi:10.1103/physrevlett.51.1550.

[45] P. Meystre, E. M. Wright, J. D. McCullen, and E. Vignes, Theory of radiation-pressure-driven interferometers, J. Opt. Soc. Am. B **2**, 1830–1840 (1985). doi:10.1364/josab.2.001830.

[46] S. Gigan et al., Self-cooling of a micromirror by radiation pressure, Nature **444**, 67–70 (2006). doi:10.1038/nature05273.

[47] O. Arcizet, P.-F. Cohadon, T. Briant, M. Pinard, and A. Heidmann, Radiation-pressure cooling and optomechanical instability of a micromirror, Nature **444**, 71–74 (2006). doi:10.1038/nature05244.

[48] J. D. Thompson et al., Strong dispersive coupling of a high-finesse cavity to a micromechanical membrane, Nature **452**, 72–75 (2008). doi:10.1038/nature06715.

[49] S. Gröblacher, K. Hammerer, M. R. Vanner, and M. Aspelmeyer, Observation of strong coupling between a micromechanical resonator and an optical cavity field, Nature **460**, 724–727 (2009). doi:10.1038/nature08171.

[50] A. D. O'Connell et al., Quantum ground state and single-phonon control of a mechanical resonator, Nature **464**, 697–703 (2010). doi:10.1038/nature08967.

[51] J. D. Teufel et al., Sideband cooling of micromechanical motion to the quantum ground state, Nature **475**, 359–363 (2011). doi:10.1038/nature10261.

[52] J. Chan et al., Laser cooling of a nanomechanical oscillator into its quantum ground state, Nature **478**, 89–92 (2011). doi:10.1038/nature10461.

[53] D. Vitali et al., Optomechanical entanglement between a movable mirror and a cavity field, Phys. Rev. Lett. **98**, 030405 (2007). doi:10.1103/physrevlett.98.030405.

[54] C. Genes, A. Mari, D. Vitali, and P. Tombesi, Robust entanglement of a micromechanical resonator with output optical fields, Phys. Rev. A **78**, 032316 (2008). doi:10.1103/physreva.78.032316.

[55] K. Hammerer et al., Strong coupling of a mechanical oscillator and a single atom, Phys. Rev. Lett. **103**, 063005 (2009). doi:10.1103/physrevlett.103.063005.

[56] C. Genes, D. Vitali, and P. Tombesi, Emergence of atom–light–mirror entanglement inside an optical cavity, Phys. Rev. A **77**, 050307(R) (2008). doi:10.1103/physreva.77.050307.

[57] M. Wallquist, K. Hammerer, P. Rabl, M. D. Lukin, and P. Zoller, Hybrid quantum devices and quantum engineering, Phys. Scr. T **137**, 014001 (2009). doi:10.1088/0031-8949/2009/t137/014001.

[58] S. Camerer, M. Korppi, A. Jöckel, D. Hunger, T. W. Hänsch, and P. Treutlein, Realization of an optomechanical interface between ultracold atoms and a membrane, Phys. Rev. Lett. **107**, 223001 (2011). doi:10.1103/physrevlett.107.223001.

[59] A. Jöckel, A. Faber, T. Kampschulte, M. Korppi, M. T. Rakher, and P. Treutlein, Sympathetic cooling of a membrane oscillator in a hybrid mechanical–atomic system, Nat. Nanotechnol. **10**, 55–59 (2015). doi:10.1038/nnano.2014.278.

[60] T. M. Karg et al., Light-mediated strong coupling between a mechanical oscillator and atomic spins 1 meter apart, Science **369**, 174–179 (2020). doi:10.1126/science.abb0328.

[61] A. Crookes, B. Yuen, and A. Demetriadou, Collective multimode strong coupling in plasmonic nanocavities, Nanophotonics **14**, 2065–2073 (2025). doi:10.1515/nanoph-2024-0618.

[62] A. Crookes, B. Yuen, and A. Demetriadou, Taming plasmonic nanocavities for persistent entanglement, Phys. Rev. B **112**, 085427 (2025). doi:10.1103/skc6-gnyr.

[63] M. A. Medina-Armendariz, R. Shabir, G. Sun, and S.-H. Dong, Study of squeezing and entanglement dynamics in a non-resonant three-level atom–optomechanical hybrid system, Phys. Lett. A **574**, 131370 (2026). doi:10.1016/j.physleta.2026.131370.